

A 6.7 GHz Methanol Maser Survey II. Low Galactic Latitudes

Kai Yang^{1,2}, Xi Chen^{1,3,4}, Zhi-Qiang Shen^{1,4}, Xiao-Qiong Li^{1,2}, Jun-Zhi Wang^{1,4}, Dong-Rong Jiang^{1,4}, Juan Li^{1,4}, Jian Dong^{1,4}, Ya-Jun Wu^{1,4}, Hai-Hua Qiao^{5,1}

ABSTRACT

We report the results of our systematic survey for Galactic 6.7 GHz Class II CH₃OH maser emission toward a sample of young stellar objects. The survey was conducted with the Shanghai Tianma Radio Telescope (TMRT). The sample consists of 3348 sources selected from the all-sky *Wide-Field Infrared Survey Explorer* (WISE) point source catalog. We have discussed the selection criteria in detail and the detection results of those at high Galactic latitudes (i.e. $|b| > 2^\circ$) in a previous paper (paper I). Here, we present the results from the survey of those at low Galactic latitudes, i.e. $|b| < 2^\circ$. Of 1875 selected WISE point sources, 291 positions that were actually associated with 224 sources were detected with CH₃OH maser emission. Among them, 32 are newly detected. Majority of the newly detected sources are associated with bright WISE sources. The majority of the detected sources ($209/224 = 93.3\%$) are quite close to the Galactic Plane ($|b| < 1^\circ$) and lie on the inner spiral arms with positive LSR velocities. Detection rate and the color-color distribution of our detection are all matched with our anticipation. Combining with detections from previous surveys, we compile a catalogue of 1085 sources with 6.7 GHz CH₃OH maser emission in our Galaxy.

Subject headings: masers — stars: formation — ISM: molecules — radio lines: ISM

1. Introduction

Methanol (CH₃OH) masers are tightly associated with massive star-forming regions in our Galaxy. There are two classes of methanol masers, Class I and Class II (Bartula et al. 1987). Unlike

¹Shanghai Astronomical Observatory, Chinese Academy of Sciences, 80 Nandan Road, Shanghai 200030, China; yangkai@shao.ac.cn, chenxi@shao.ac.cn, zshen@shao.ac.cn.

²University of Chinese Academy of Sciences, 19A Yuquanlu, Beijing 100049, China.

³Center for Astrophysics, Guangzhou University, Guangzhou 510006, China; chenxi@gzhu.edu.cn.

⁴Key Laboratory of Radio Astronomy, Chinese Academy of Sciences, China.

⁵National Time Service Center, Chinese Academy of Sciences, Xi'an, Shaanxi, 710600, China

Class I methanol masers (e.g., transitions at 44 GHz and 95 GHz) which are pumped by collision excitation at different positions separated by ~ 1 pc from high-mass young stellar objects (YSOs, Voronkov et al. 2010, 2014), Class II methanol masers, pumped by infrared radiation, are commonly found close to YSOs (Caswell et al. 2010). The $5_1 \rightarrow 6_0$ A⁺ 6.7 GHz methanol maser is a well-known Class II methanol maser. It is widespread in the Milky Way and is the second strongest known maser, only exceeded by the 22 GHz water maser (Menten 1991). Different from other species of masers (OH, H₂O and SiO masers), the 6.7 GHz CH₃OH maser is exclusively associated with massive star-forming regions (Minier et al. 2003; Ellingsen 2006; Xu et al. 2008), making it an excellent tool for studying massive star-forming regions (e.g. Ellingsen 2007). In addition, the VLBI astrometry of the 6.7 GHz methanol maser can obtain the model-independent distance measurements for the study on the structures of our Galaxy (Reid et al. 2009).

Methanol masers at the 6.7 GHz transition have been detected towards more than 1,000 sources to date. Many surveys, including unbiased surveys and targeted surveys, have been conducted to search for the 6.7 GHz methanol maser (e.g. MacLeod et al. 1992; Caswell et al. 1995a; Caswell 1996; Ellingsen et al. 1996; van der Walt et al. 1996; Walsh et al. 1997; Ellingsen 2007). As an unbiased survey, the Parkes Methanol Multibeam (MMB) Survey of a region of $186^\circ < |l| < 60^\circ$ and $|b| < 2^\circ$ (Caswell et al. 2010; Green et al. 2010; Caswell et al. 2011; Green et al. 2012; Breen et al. 2015) detected 954 sources, including 344 new detections.

Since 2015, we have performed a systematic 6.7 GHz Class II methanol maser survey toward targets selected from the all-sky *Wide-Field Infrared Survey Explorer* (WISE) point source catalog. This WISE point catalogue is a relatively new database and covers the entire sky (Wright et al. 2010), which makes it ahead of several other infrared surveys and best candidate for us to construct a targeted sample. Our survey was conducted with the Shanghai Tianma Radio Telescope (TMRT). In a previous paper (Yang et al. 2017, hereafter Paper I), we reported the survey results for the selected sources at high Galactic latitude ($|b| > 2^\circ$); there are 3 new sources among the 12 detected sources. Here we present the remaining 6.7 GHz methanol maser survey results for those at low Galactic latitudes ($|b| < 2^\circ$). We briefly describe the sample and observations in Section 2. The results are presented in Section 3, followed by discussions in Section 4 and a summary in Section 5.

2. Sample and Observations

The sample selection is fully detailed in Paper I. Here, we just recap some key points in constructing the sample from the WISE point catalog. We first pick out 473 WISE point sources which are associated with the MMB 6.7 GHz methanol maser catalog sources, with all the magnitudes available in the 4 WISE-bands. Because 265 sources from Breen et al. (2015) in the region of

$20^\circ < |l| < 60^\circ$ and $|b| < 2^\circ$ were not published at that time, the MMB 6.7 GHz methanol maser catalog only contains 684 sources located in the region of $186^\circ < |l| < 20^\circ$ and $|b| < 2^\circ$. Statistical analysis of the magnitude and color-color of these 473 sources shows that most (455/473=96%) of the known CH₃OH masers meet the criteria of magnitude: $[3.4] < 14$ mag, $[4.6] < 12$ mag, $[12] < 11$ mag and $[22] < 5.5$ mag and the majority of them (330/473=73%) meet the criteria of color: $[3.4] - [4.6] > 2$, and $[12] - [22] > 2$.

Applying these selection criteria to the all-sky WISE catalog, we found about 13,000 candidate WISE sources that may be associated with CH₃OH masers. After excluding those already detected in the Parkes MMB survey region ($186^\circ < |l| < 20^\circ$, $|b| < 2^\circ$), we finally built up a sample of 3348 WISE sources with declination above -30° . The sample can be divided into 2 sub-samples. One sub-sample includes 1473 sources which locate at high Galactic latitude region with $|b| > 2^\circ$, and the results of the 6.7 GHz methanol survey have been published in Paper I. The other sub-sample consists of 1873 sources, which are located at the low Galactic latitude region with $|b| < 2^\circ$ (Table 1).

We performed this 6.7 GHz methanol maser survey at low Galactic latitudes between 2016 June and 2018 January with the TMRT. The TMRT is a newly built and fully steerable radio telescope with a diameter of 65 m in Shanghai, China. A cryogenically cooled C-band receiver with a frequency range of 4–8 GHz and the Digital Backend System (DIBAS) were used to record signals. A spectral window of a bandwidth of 23.4 MHz was used to cover the rest frequency of the CH₃OH maser line, 6.6685192 GHz. This window has 16,384 channels with a spectral resolution of 1.431 kHz (or a velocity resolution is about 0.09 km s⁻¹). The system temperature is 20–30 K and the aperture efficiency of the TMRT is $\sim 55\%$, resulting in a sensitivity of 1.5 Jy K⁻¹. The beam size is $\sim 3'$ (HPBW) at the frequency of 6.7 GHz.

In our observations, position-switching mode was used and each source was observed in two ON–OFF cycles, with each cycle of 4 minutes. The OFF position was set to $(0.0^\circ, -0.4^\circ)$ from the ON position in (R.A., decl.). We observed W3(OH) and NGC7538 as flux density calibrators with an uncertainty of less than 20%.

The GILDAS/CLASS package was used to conduct the data reduction. We fitted and subtracted the linear baseline of the spectrum. The root-mean-square (rms) noise is about 50–80 mJy.

For those detected methanol maser sources with a wide velocity range of >30 km s⁻¹ (eight in total, see Section 3), we further carried out the on-the-fly (OTF) (Dong et al. 2016, 2018a,b) mapping observation to determine positions of separated CH₃OH masers (see Section 3.2).

3. Results

Single point observations with the TMRT detected 291 sources with the 6.7 GHz CH_3OH maser emission. In our survey, eight sources (G28.287–0.348, G30.788+0.203, G30.789+0.232, G30.823+0.134, G31.221+0.020, G31.253+0.003, G33.092–0.073, and G33.143–0.088) have a wide velocity range of $>30 \text{ km s}^{-1}$ with methanol spectral features clearly separated. We further conducted OTF observations towards these sources to determine the maser positions of the different emission shown in their spectra. Results from the single point observations are described in Section 3.1, and the OTF observations in Section 3.2.

3.1. Detections from the single-point observations

In total, TMRT survey of those at low Galactic latitudes detected 6.7 GHz CH_3OH masers from 291 positions which are actually from 224 sources because some close positions show similar methanol spectral features and thus are identified with a same origin. Comparison with previous surveys showed that 32 sources are newly detected. Figure 1 displays the spectra of these newly-identified CH_3OH masers and their properties are detailed in Table 2. The spectra and properties of previously detected sources (192 in total) are shown in Figure 2 and Table 3, respectively.

For the eight sources from our survey with a very wide velocity range ($>30 \text{ km s}^{-1}$, see above), we can clearly see that the left and right parts of their spectra locate at separated positions from different regions after taking our OTF observation into account (see Section 3.2), so we only discuss their separated parts instead of their whole spectra and we name the different part of their spectra by adding the position in the spectra after their Galactic coordinate as one source, like G31.221+0.020(Left).

Each velocity component of the 6.7 GHz CH_3OH maser usually has a velocity range of $0.1\text{--}3 \text{ km s}^{-1}$ (Bartkiewicz et al. 2016), so sources showing wide velocity ranges may have more components. The smallest velocity range of the detected sources is 0.47 km s^{-1} (G43.089–0.011 and G75.010+0.274) with a single feature while the largest is 24.4 km s^{-1} (G43.148+0.013). The median velocity range is 5.5 km s^{-1} and 11 sources have a velocity range larger than 16 km s^{-1} .

The median peak flux density of our 224 detected sources is 3.0 Jy. G23.010–0.410 has the strongest peak flux density of 406.2 Jy. The weakest peak flux density is 0.23 Jy from source G30.980+0.216. There are 36 sources having a peak flux density higher than 20 Jy and 59 sources with a peak flux density lower than 1.0 Jy. Among the 32 newly detected sources, the strongest source is G82.308+0.729 and the weakest source is G25.177+0.211 with a peak flux density of 58.4 and 0.31 Jy, respectively. Most of them (28/32) have a peak flux density lower than 2.0 Jy.

Among the 192 previously detected sources, 167 sources were detected by the Parkes MMB survey (Breen et al. 2015). The remaining 25 sources were detected by other surveys. Since our observations were conducted with the single-dish telescope, the positions are not exactly same as the previous detections. Thus, we only present the information on the variations of their spectral profiles. The details of their spectral profile changes are listed in Table 4.

3.2. Maser positions determined from the OTF observations

Eight sources (described above in Section 3.1) show a wide velocity range in their methanol spectra, we observed them with the OTF mode in order to figure out the maser distribution due to their obviously separated spectral features in left and right parts. Among them, the left and right parts of G30.788+0.203 and G30.789+0.232, G31.221+0.020 and G31.253+0.003, G33.092–0.073 and G33.143–0.088 share similar features respectively, so we observed toward five positions with the OTF observations. The center coordinates and the side length of the square regions chosen for the OTF observations towards five positions are listed in Table 5. We also list the maser positions determined from the OTF mapping observations in each region along with the positional offset of associated MMB sources decided by ATCA in Table 5. Taking the pointing error of TMRT ($\sim 10''$) and the fitting error from the OTF observation ($\sim 10''$) into consideration, our TMRT OTF observations have a positional accuracy better than $20''$. Comparing with the positions determined by the ATCA observations, we found that the positional accuracy achieved from our TMRT OTF observations is better than $10''$ towards six sources (see Table 5). The other three maser sources show larger position offsets ($10'' \sim 20''$) with regard to the ATCA measurements, but this is consistent with the estimated positional accuracy of less than $20''$ from the TMRT OTF mapping observations. Figure 3 shows the velocity-integrated intensity map from the OTF observation. We can see that the left and right parts (middle parts) of each source are all from two (three) different positions and we will discuss them as different sources.

4. Discussions

4.1. Newly detected sources

Although the Parkes MMB survey is an unbiased survey, we still detected 18 new sources towards the MMB region ($20^\circ < |l| < 60^\circ$, $|b| < 2^\circ$) also covered by the MMB survey. The variability of the 6.7 GHz methanol masers may contribute to the new detections. Several proposed mechanisms may explain its variability: (i) pulsation of a young high-mass star (Inayoshi et al. 2013; Sanna et al. 2015), (ii) rotating spiral shocks from hot and dense material in the central

gap of the circumbinary accretion disc (Parfenov & Sobolev 2014), (iii) periodic accretion of a protostar or accretion disc (Araya et al. 2010), (iv) a colliding-wind binary (CWB) system (van der Walt et al. 2009, 2016), (v) an eclipsing binary (Maswanganye et al. 2015). Recently, there are several luminous bursts in high-mass star formation (e.g. Caratti o Garatti et al. 2017; Hunter et al. 2017, 2018; Szymczak et al. 2018), episodic accretion due to disk fragmentation (Meyer et al. 2017) may be a dominant mechanism for such bursts. Notably, the spectral profile of the 6.7 GHz CH₃OH maser can even change in a timescale of a few days (Caswell et al. 1995b). In addition, these new sources may also be due to a better sensitivity of the TMRT survey with a rms noise of 0.05 Jy compared to a typical rms noise level of 0.07 Jy in the MMB survey and 0.06 Jy to 4 Jy of other previous surveys.

For the 32 newly detected sources, we show their infrared WISE three-color images in Figure 4. Five sources (G24.362–0.146, G31.253+0.003(Left), G35.225–0.360, G49.537–0.904, and G75.010+0.274) locate in the infrared dark cloud. Most of the newly detected sources, $27/32 = 84.4\%$, are associated with bright WISE sources. There are also six sources (G76.093+0.158, G78.969+0.541, G84.193+1.439, G84.951–0.691, G84.984–0.529, and G124.015–0.027) that are bright in the infrared environment but not in the infrared dark cloud. The remaining 21 sources have bright point counterparts in the infrared dark cloud.

The ATLASGAL (APEX Telescope Large Area Survey of the Galaxy) survey imaged the Galactic plane in a region of $-60^\circ < |l| < 60^\circ$ and $|b| < 1.5^\circ$ at $870 \mu\text{m}$ with the APEX Telescope in its first step (Schuller et al. 2009). Urquhart et al. (2014) combined the ATLASGAL survey and the Red Midcourse Space Experiment Source (RMS) surveys, and identified a sample which contains ~ 1300 clumps associated with ~ 1700 embedded massive young protostars. We have 18 maser sources located in the overlapped region of $20^\circ < |l| < 60^\circ$, $|b| < 1.5^\circ$ from the 32 newly detected sources. Among these 18 sources, 12 sources have been found to be associated clumps (see Table 2). After excluding extended emission with a multiscale decomposition tool and using a Gaussian source-fitting algorithm (MRE-GCL), Csengeri et al. (2014) identified 10861 compact submillimeter sources also from the ATLASGAL survey in the region of $|l| < 60^\circ$, $|b| < 1.5^\circ$ and $-80^\circ < l < -60^\circ$, $-2^\circ < b < 1^\circ$. 14 sources are found associated sources among the 18 sources. In addition to this, Urquhart et al. (2013) presented a sample of molecular clumps containing compact and ultracompact H II regions in the area of $10^\circ < l < 60^\circ$, $b < 1^\circ$ by combining the ATLASGAL survey and the CORNISH (Co-Ordinated Radio 'N' Infrared Survey for High-mass star formation) project. But we have not found any associated regions. There have been many surveys conducted by the Very Large Array (VLA) at 6cm (Law et al. 2008; Urquhart et al. 2009) searching for compact sources, and several observations conducted by the Atacama Large Millimetre/submillimetre Array (ALMA) towards the sources from the ATLASGAL survey which are considered to be young massive clumps (Chibueze et al. 2017; Csengeri et al. 2017a,b, 2018), but we have not found sources associated with the sources we newly detected. In conclusion, our

newly detected sources may be in the early evolutionary stage of star-formation, and the successive observation of their variation will also give us a better understanding of this period of star forming.

4.2. Detection rate versus Galactic longitude and WISE color

4.2.1. Detection rate

In our survey, a detection rate of $224/1875 = 11.9\%$ was achieved towards the WISE–selected sources with magnitudes and colors described in Section 2. We can derive an expected detection rate using the methanol maser and WISE-selected source data in the MMB survey region. For a single dish survey, such as the Parkes MMB survey, any targets that lie within the FWHM of the telescope could be detected by a single point observation. Moreover, since the complicated background emission around the Galactic center might affect WISE source selection, we exclude the WISE sources towards the Galactic center region with $|l| < 10^\circ$. As such, the number of selected WISE sources is about 3,700 in the above-mentioned MMB survey region ($186^\circ < |l| < 20^\circ$, $|b| < 2^\circ$, and without the Galactic center) after taking the beam coverage factor into account. Within such a region, there are 280 CH_3OH maser sources detected by the MMB survey which meet the WISE selection criteria, while the total number of the 6.7 GHz CH_3OH maser sources which have WISE sources with 4-band flux density measurements is 388. The total number of the 6.7 GHz CH_3OH masers in this region is 528. Thus we can derive a detection rate of $280/3700 \times 528/388 = 10.3\%$ towards the WISE sources with the criteria. Therefore, the actual detection rate (11.9%) in our survey is quite consistent with the expected rate (10.3%) using the blind MMB survey data.

Our survey and the Parkes MMB survey have an overlap region, $20^\circ < |l| < 60^\circ$, $|b| < 2^\circ$. The Parkes MMB survey detected 265 sources in this region. Among the 189 sources we detected in this region, there are 167 sources associated with MMB detections. From our sample selection in Paper I, almost all (96%) of the known methanol masers meet the magnitude criteria and 73% of the them meet the color criteria, the proportion of our detected sources that are associated with MMB sources in the MMB sources is $96\% \times 73\% = 70.1\%$. The true rate is $167/265 = 63.0\%$ which is less than the estimated rate. 22 new sources we detect are mainly due to our better sensitivity. If considering these 22 sources, the actual detection rate will be $189/265 = 71.3\%$, which is well consistent with the estimated rate.

4.2.2. *Detection rate versus Galactic longitude*

To investigate the relationship between the detection rate and Galactic longitude distribution of our survey, we divided our 1875 sample sources and 224 detected CH₃OH masers along their Galactic longitudes and calculated the detection rate every 5° bin of longitude. A histogram of sample source number and detection number are shown in the upper panel of Figure 5. The corresponding detection rate is given in the lower panel of Figure 5. Overall, it is clearly seen that the detection rate of methanol maser decreases with the Galactic longitude from 20° to 180°. The sources in the Galactic center region of 20° – 40° are located in the 1st Quad molecular cloud where the inner spiral arms lie on (Dame et al. 2001), thus having strong star formation activity and near distance will result in high appearance chance of methanol maser. The number becomes much lower in other regions. The Cygnus X and Cas A molecular clouds around the Galactic longitude of 80° and 110° contribute to the appearance of several methanol sources and the increase of the detection rate. These all show that the detection rate and the distribution of CH₃OH maser sources are both in good agreement with the presence of molecular clouds where high mass star-forming regions rise. Due to the small number of sample sources at Galactic longitude of >120°, we do not discuss the detection rate.

4.2.3. *Detection rate versus WISE color*

Since our sample sources are selected with a certain criteria of the WISE color, $[3.4] - [4.6] > 2$ and $[12] - [22] > 2$, we can compare the color-color diagram of the detected sources and the sample sources in the upper panel of Figure 6. From the distribution of the black dots (sample sources) and the red dots (detected sources), we found they almost share the similar infrared characteristic. In order to study their infrared environment of our detected sources, the numbers of sample sources and detected sources and detection rate along every 0.2 color are shown in the lower panels of Figure 6. The numbers of sample sources decrease with $[3.4] - [4.6]$ color, but have a peak at ~ 3.3 with $[12] - [22]$ color. The number of detected sources show the similar distribution of the number of sample sources. The detection rates along $[3.4] - [4.6]$ color have a fluctuation around 15% and those along $[12] - [22]$ color show a rising trend.

4.3. Galactic distribution

4.3.1. Our detection

The Galactic latitude distribution of our detected 224 sources is shown in Figure 7. Because the region of $186^\circ \leq l \leq 20^\circ$ had been included by the Parkes MMB survey before our sample selection, we observed the rest region with $20^\circ < |l| < 186^\circ$ and $|b| < 2^\circ$. Most of the detected sources, $208/224 = 92.9\%$, locate at regions of $|b| < 1^\circ$. Only 16 sources have a Galactic latitude larger than 1° . Among them, 3 sources (G84.193+1.439, G89.930+1.669 and G99.070+1.200) are newly detected. In the MMB survey, there are $893/954 = 93.6\%$ sources with a Galactic latitude of $|b| < 1^\circ$, which is consistent with our survey.

The LSR velocities of our detected sources versus Galactic longitude are shown in Figure 8 (middle, blue and red dots). As 6.7 GHz methanol maser is only associated with high-mass star-forming regions and thus is a good tracer of spiral structures in the Milky Way (Reid et al. 2014, 2016), the detected sources can be derived from different spiral arms. After combining the estimated kinematic distances derived from the Galactic rotation model in Reid et al. (2014), we found that sources in the $20^\circ - 60^\circ$ longitude region have positive LSR velocities and they are mostly stay on the spiral arms of Perseus, Carina-Sagittarius, Crux-Scutum and Norma. According to the estimated distances, the positions of these detected sources are plotted in Figure 9. Sources in the $60^\circ - 186^\circ$ longitude region mostly have negative LSR velocities and they are mainly locate on the spiral arms of Perseus and Norma.

4.3.2. All known 6.7 GHz methanol maser sources

Many Galactic 6.7 GHz CH_3OH maser surveys have been conducted in the last 20 years. By combining survey results from the literature (Pestalozzi et al. 2005; Ellingsen 2007; Pandian et al. 2007; Xu et al. 2008; Cyganowski et al. 2009; Caswell et al. 2010, 2011; Green et al. 2010, 2012; Szymczak et al. 2012; Olmi et al. 2014; Breen et al. 2015; Yang et al. 2017), we compiled a catalogue of 1085 sources at 6.7 GHz Class II CH_3OH masers (Table 6). Their galactic distribution, LSR velocity as a function of Galactic longitude, and the source number count as a function of Galactic latitude and longitude are presented in Figure 8.

Among these 1085 6.7 GHz methanol masers, there are 404 sources located in the $0^\circ - 40^\circ$ longitude region, and 407 in the opposite longitude $320^\circ - 360^\circ$ region ($-40^\circ - 0^\circ$). As a result, most of the 6.7 GHz methanol masers, $811/1085 = 74.7\%$, are located in the above two regions and the maser distribution is the most abundance in the regions. From the distribution of the LSR velocity versus Galactic longitude in Fig. 8 (middle), we find that most of the sources within the 0°

-40° longitude region show positive velocities and most sources in the $-40^\circ - 0^\circ$ longitude region have negative velocities. Sources in these two regions show peak velocities at Galactic longitude of $\sim 30^\circ$ and $\sim -30^\circ$, respectively. These two opposite Galactic longitude regions locate near the Galactic center including the inner and the most compact parts of some main spiral arms in our Galaxy. Sources with the peak velocity at Galactic longitude of $\sim 30^\circ$ and $\sim -30^\circ$ locate on the Crux-Scutum arm and Norma arm, respectively. The peak may trace the interacting region of the Galactic bar and the Crux-Scutum arm and Norma arms. Due to the 344 newly detected sources in the Parkes MMB survey (Caswell et al. 2010; Green et al. 2010; Caswell et al. 2011; Green et al. 2012; Breen et al. 2015), there are now more sources in the Galactic region of $-20^\circ - 20^\circ$, compared to the Galactic longitude distribution in Pestalozzi et al. (2005).

Most of the known 6.7 GHz methanol masers (1068/1085=98.4%) are located in the regions of $|b| < 2^\circ$, and they are mostly found around $|b| < 1^\circ$, revealing that 6.7 GHz methanol masers prefer to being associated with the star formation in the Galactic Plane. Besides the previous surveys were mostly conducted towards the Galactic Plane, the star forming cluster environment is much more complicated at low latitudes, hence much more gases and dusts which are essential for star-forming activity. Therefore, it should be the case that the most 6.7 GHz CH_3OH masers are located at low latitudes around the Galactic Plane. We simulated a Gaussian fit with an FWHM of 0.56° to the Galactic latitude distribution of methanol masers, which is consistent with the Gaussian fit with an FWHM of 0.52° in Pestalozzi et al. (2005).

5. Summary

With the newly built TMRT, we performed a systematic survey of 6.7 GHz CH_3OH masers towards 1875 sources at low Galactic latitudes ($|b| < 2^\circ$). These sources are selected from the all-sky WISE point catalog with a certain criteria of magnitude and color. There are 32 new detections among 224 detected sources. Their spectra have peak flux densities of 0.23 Jy to 406.2 Jy and their velocity ranges have a range of 0.47 km s^{-1} to 24.4 km s^{-1} . The source number along the Galactic latitude shows that most of them are located at even lower Galactic latitude, $|b| < 1^\circ$. Their distribution and LSR velocities are associated with the presence of spiral arms and molecular clouds. The detection rates along the Galactic longitude and color meet our anticipation. We also present a compiled catalog containing all 1085 6.7 GHz methanol masers known to date.

Acknowledgements

We are thankful for the assistance from the operators of the TMRT during the observations. This work was supported by the National Natural Science Foundation of China (11590780, 11590781, 11590784 and 11873002), the Knowledge Innovation Program of the Chinese Academy of Sciences (Grant No. KJCX1-YW-18), the Scientific Program of Shanghai Municipality (08DZ1160100), and Key Laboratory for Radio Astronomy, CAS. K. Yang would like to thank the China Scholarship Council (CSC) for the support. H.-H. Q. is partially supported by the Special Funding for Advanced Users, budgeted and administrated by Center for Astronomical Mega-Science, Chinese Academy of Sciences (CAMS-CAS) and CAS “Light of West China” Program.

REFERENCES

- Araya, E. D., Hofner, P., Goss, W. M., et al. 2010, *ApJ*, 717, L133 [6]
- Bartkiewicz, A., Szymczak, M., & van Langevelde, H. J. 2016, *A&A*, 587, A104 [4]
- Batrla, W., Matthews, H. E., Menten, K. M., & Walmsley, C. M. 1987, *Nature*, 326, 49 [1]
- Breen, S. L., Fuller, G. A., Caswell, J. L., et al. 2015, *MNRAS*, 450, 4109 [2, 5, 9, 10, 17, 24]
- Caratti o Garatti, A., Stecklum, B., Garcia Lopez, R., et al. 2017, *Nature Physics*, 13, 276 [6]
- Caswell, J. L. 1996, *MNRAS*, 283, 606 [2]
- Caswell, J. L., Fuller, G. A., Green, J. A., et al. 2010, *MNRAS*, 404, 1029 [2, 9, 10]
- Caswell, J. L., Fuller, G. A., Green, J. A., et al. 2011, *MNRAS*, 417, 1964 [2, 9, 10]
- Caswell, J. L., Vaile, R. A., & Ellingsen, S. P. 1995, *PASA*, 12, 37 [6]
- Caswell, J. L., Vaile, R. A., Ellingsen, S. P., Whiteoak, J. B., & Norris, R. P. 1995, *MNRAS*, 272, 96 [2]
- Chibueze, J. O., Csengeri, T., Tatematsu, K., et al. 2017, *ApJ*, 836, 59 [6]
- Csengeri, T., Bontemps, S., Wyrowski, F., et al. 2017, *A&A*, 600, L10 [6]
- Csengeri, T., Bontemps, S., Wyrowski, F., et al. 2017, *A&A*, 601, A60 [6]
- Csengeri, T., Bontemps, S., Wyrowski, F., et al. 2018, *A&A*, 617, A89 [6]
- Csengeri, T., Urquhart, J. S., Schuller, F., et al. 2014, *A&A*, 565, A75 [6, 17]

- Cyganowski, C. J., Brogan, C. L., Hunter, T. R., & Churchwell, E. 2009, *ApJ*, 702, 1615 [9]
- Dame, T. M., Hartmann, D., & Thaddeus, P. 2001, *ApJ*, 547, 792 [8]
- Dong, J., Fu, L., Liu, Q., & Shen, Z. 2018, *Experimental Astronomy*, 45, 397 [3]
- Dong, J., Wu, Y. J., Yuan, J., et al. 2016, *Progress in Astronomy*, 34, 212 [3]
- Dong, J., Zhong, W., Wang, J., Liu, Q., & Shen, Z. 2018, *IEEE Transactions on Antennas and Propagation*, 66, 2044 [3]
- Ellingsen, S. P. 2006, *ApJ*, 638, 241 [2]
- Ellingsen, S. P. 2007, *MNRAS*, 377, 571 [2, 9]
- Ellingsen, S. P., von Bibra, M. L., McCulloch, P. M., et al. 1996, *MNRAS*, 280, 378 [2]
- Green, J. A., Caswell, J. L., Fuller, G. A., et al. 2010, *MNRAS*, 409, 913 [2, 9, 10, 46]
- Green, J. A., Caswell, J. L., Fuller, G. A., et al. 2012, *MNRAS*, 420, 3108 [2, 9, 10]
- Hunter, T. R., Brogan, C. L., MacLeod, G., et al. 2017, *ApJ*, 837, L29 [6]
- Hunter, T. R., Brogan, C. L., MacLeod, G. C., et al. 2018, *ApJ*, 854, 170 [6]
- Inayoshi, K., Sugiyama, K., Hosokawa, T., Motogi, K., & Tanaka, K. E. I. 2013, *ApJ*, 769, L20 [5]
- Law, C. J., Yusef-Zadeh, F., & Cotton, W. D. 2008, *ApJS*, 177, 515 [6]
- MacLeod, G. C., Gaylard, M. J., & Nicolson, G. D. 1992, *MNRAS*, 254, 1P [2]
- Maswanganye, J. P., Gaylard, M. J., Goedhart, S., Walt, D. J. v. d., & Booth, R. S. 2015, *MNRAS*, 446, 2730 [6]
- Menten, K. M. 1991, *ApJ*, 380, L75 [2]
- Meyer, D. M.-A., Vorobyov, E. I., Kuiper, R., & Kley, W. 2017, *MNRAS*, 464, L90 [6]
- Minier, V., Ellingsen, S. P., Norris, R. P., & Booth, R. S. 2003, *A&A*, 403, 1095 [2]
- Olmi, L., Araya, E. D., Hofner, P., et al. 2014, *A&A*, 566, A18 [9]
- Pandian, J. D., Goldsmith, P. F., & Deshpande, A. A. 2007, *ApJ*, 656, 255 [9]
- Parfenov, S. Y., & Sobolev, A. M. 2014, *MNRAS*, 444, 620 [6]

- Pestalozzi, M. R., Minier, V., & Booth, R. S. 2005, *A&A*, 432, 737 [9, 10]
- Reid, M. J., Dame, T. M., Menten, K. M., & Brunthaler, A. 2016, *ApJ*, 823, 77 [9]
- Reid, M. J., Menten, K. M., Zheng, X. W., et al. 2009, *ApJ*, 700, 137 [2, 17]
- Reid, M. J., Menten, K. M., Brunthaler, A., et al. 2014, *ApJ*, 783, 130 [9, 17]
- Sanna, A., Menten, K. M., Carrasco-González, C., et al. 2015, *ApJ*, 804, L2 [5]
- Schuller, F., Menten, K. M., Contreras, Y., et al. 2009, *A&A*, 504, 415 [6]
- Szymczak, M., Olech, M., Wolak, P., Gérard, E., & Bartkiewicz, A. 2018, *A&A*, 617, A80 [6]
- Szymczak, M., Wolak, P., Bartkiewicz, A., & Borkowski, K. M. 2012, *Astronomische Nachrichten*, 333, 634 [9, 17, 24]
- Urquhart, J. S., Hoare, M. G., Purcell, C. R., et al. 2009, *A&A*, 501, 539 [6]
- Urquhart, J. S., Moore, T. J. T., Csengeri, T., et al. 2014, *MNRAS*, 443, 1555 [6, 17]
- Urquhart, J. S., Thompson, M. A., Moore, T. J. T., et al. 2013, *MNRAS*, 435, 400 [6]
- van der Walt, D. J., Goedhart, S., & Gaylard, M. J. 2009, *MNRAS*, 398, 961 [6]
- van der Walt, D. J., Maswanganye, J. P., Etoke, S., Goedhart, S., & van den Heever, S. P. 2016, *A&A*, 588, A47 [6]
- van der Walt, D. J., Retief, S. J. P., Gaylard, M. J., & MacLeod, G. C. 1996, *MNRAS*, 282, 1085 [2]
- Voronkov, M. A., Caswell, J. L., Ellingsen, S. P., Green, J. A., & Breen, S. L. 2014, *MNRAS*, 439, 2584 [2]
- Voronkov, M. A., Caswell, J. L., Ellingsen, S. P., & Sobolev, A. M. 2010, *MNRAS*, 405, 2471 [2]
- Walsh, A. J., Hyland, A. R., Robinson, G., & Burton, M. G. 1997, *MNRAS*, 291, 261 [2]
- Wright, E. L., Eisenhardt, P. R. M., Mainzer, A. K., et al. 2010, *AJ*, 140, 1868-1881 [2]
- Xu, Y., Li, J. J., Hachisuka, K., et al. 2008, *A&A*, 485, 729 [2, 9]
- Yang, K., Chen, X., Shen, Z. Q., et al. 2017, *ApJ*, 846, 160 (Paper I) [2, 9]

Table 1: WISE–Selected sources for the TMRT survey of methanol maser

Number	l ($^{\circ}$)	b ($^{\circ}$)	R.A. (J2000) (h m s)	Decl. (J2000) ($^{\circ}$ ' ")	w1 (3.4 μ m) (mag)	w2 (4.6 μ m) (mag)	w3 (12 μ m) (mag)	w4 (22 μ m) (mag)	w1–w2 (mag)	w3–w4 (mag)
(1)	(2)	(3)	(4)	(5)	(6)	(7)	(8)	(9)	(10)	(11)
1	20.234	0.085	18:27:39.95	–11:14:32.3	12.940	8.873	6.925	3.186	4.067	3.739
2	20.363	–0.014	18:28:16.02	–11:10:25.4	13.167	10.206	5.805	1.167	2.961	4.638
3	20.762	–0.064	18:29:12.19	–10:50:36.0	6.458	4.428	0.890	–1.821	2.030	2.711
4	20.926	–0.050	18:29:27.80	–10:41:28.8	11.144	7.433	4.516	1.576	3.711	2.940
5	21.023	–0.063	18:29:41.54	–10:36:42.5	13.182	9.106	4.360	1.017	4.076	3.343
6	21.370	–0.226	18:30:56.20	–10:22:48.7	9.588	7.408	5.919	2.130	2.180	3.789
7	22.050	0.211	18:30:38.52	–09:34:28.2	14.712	10.219	7.869	3.357	4.493	4.512
8	22.355	0.066	18:31:44.05	–09:22:17.3	9.174	7.028	3.763	0.036	2.146	3.727
9	23.010	–0.410	18:34:40.25	–09:00:38.2	11.475	6.966	6.050	0.072	4.509	5.978
10	23.185	–0.380	18:34:53.23	–08:50:27.4	13.677	10.738	8.320	5.712	2.939	2.608
									

Table 2.: 32 newly detected 6.7 GHz methanol masers.

Name (gl, gb) ($^{\circ}$, $^{\circ}$) (1)	R.A. (J2000) (h m s) (2)	DEC (J2000) ($^{\circ}$ $'$ $''$) (3)	ΔV (km s $^{-1}$) (4)	v_p (km s $^{-1}$) (5)	S_p (Jy) (6)	S_l (Jy km s $^{-1}$) (7)	Epoch yy/mm/dd (8)	Distance kpc (9)	Only one features? (10)	Other name (11)
G24.273-0.137	18:36:02.31	-07:45:48.5	88.7, 101.4	100.9	1.04	0.44	1608/07			
G24.313-0.154	18:36:10.51	-07:44:06.1	99.6, 101.5	100.9	2.03	0.90	1608/07	5.91	N	AGAL024.311-00.154/G024.3123-0.1543
G24.362-0.146	18:36:14.34	-07:41:19.3	54.8, 55.9	55.3	1.86	0.70	1608/07	3.67	Y	
G24.633+0.153	18:35:40.11	-07:18:34.8	112.7, 118.7	114.3	1.22	0.45	1609/05	7.36	N	AGAL024.633+00.152/G024.6316+0.1526
G25.177+0.211	18:36:28.20	-06:48:00.7	99.9, 102.1	100.5	0.31	0.24	1609/05	8.96	N	AGAL025.178+00.211/G025.1774+0.2102
G28.804-0.023	18:43:58.88	-03:40:59.6	100.3, 102.6	101.3	0.54	0.62	1609/16	7.96	N	AGAL028.802-00.022/G028.8030-0.0214
G29.281-0.330	18:45:56.85	-03:23:56.4	91.6, 93.1	92.4	1.86	1.09	1609/16	4.84	Y	AGAL029.281-00.331/G029.2819-0.3313
G31.221+0.020(Left)	18:48:14.70	-01:30:49.1	79.6, 80.3	80.1	0.41	0.15	1608/03	4.66	Y	AGAL031.221+00.021/G031.22210+0.0203
G31.253+0.003(Left)	18:48:21.93	-01:29:36.0	36.7, 42.0	37.4	0.50	0.25	1608/03	2.06	N	AGAL031.251+00.002/G031.2511+0.0040
G33.229-0.018	18:52:02.71	+00:15:20.6	92.1, 98.2	92.4	0.48	0.15	1608/19	6.22	N	G033.2278-0.0179
G33.425-0.315	18:53:27.46	+00:17:41.7	45.3, 46.4	46.0	0.55	0.28	1609/22	2.20	Y	
G35.149+0.809	18:52:36.09	+02:20:31.6	71.7, 72.5	72.0	0.68	0.23	1609/22	4.66	Y	AGAL035.149+00.809/G035.1493+0.8099
G35.225-0.360	18:56:54.24	+01:52:35.7	59.1, 60.0	59.7	0.62	0.23	1609/22	10.21	Y	AGAL035.226-00.359/G035.2266-0.3587
G43.089-0.011	19:10:09.53	+09:01:26.8	8.80, 9.27	9.06	0.33	0.10	1611/14	11.46	Y	
G49.537-0.904	19:25:42.16	+14:18:22.1	39.2, 41.9	39.6	0.63	0.20	1609/11	3.25	N	G049.5444-0.8830
G53.485+0.521	19:28:19.07	+18:27:22.2	54.0, 54.5	54.2	0.32	0.10	1609/29	4.04	Y	AGAL053.496+00.522/G053.4850+0.5221
G54.371-0.613	19:34:18.73	+18:41:13.8	34.9, 38.2	37.9	0.81	0.32	1703/06	3.92	N	AGAL054.373-00.614/G054.3721-0.6140
G59.436+0.820	19:39:34.20	+23:48:25.5	-50.4, -47.5	-50.2	0.35	0.10	1609/29	11.95	N	
G59.498-0.236	19:43:42.45	+23:20:13.8	27.1, 28.5	27.5	0.62	0.50	1608/19	3.49	N	AGAL059.497-00.236/G059.4972-0.2358
G62.310+0.114	19:48:35.35	+25:56:41.8	23.4, 25.9	23.6	0.46	0.13	1608/04	3.19	N	
G74.098+0.110	20:17:56.32	+35:55:24.3	-6.63, 1.03	-0.22	5.19	2.85	1609/24	4.25	N	
G75.010+0.274	20:19:49.29	+36:46:09.4	3.06, 3.53	3.36	0.53	0.11	1609/25	3.84	Y	
G76.093+0.158	20:23:23.65	+37:35:34.3	4.27, 6.90	4.92	0.49	0.22	1610/02	3.72	N	
G78.969+0.541	20:30:22.77	+40:09:23.2	4.01, 5.48	4.74	1.24	0.88	1609/16	2.87	N	
G81.794+0.911	20:37:47.39	+42:38:39.0	-4.73, 7.54	7.19	0.59	0.14	1608/18	2.87	N	
G82.308+0.729	20:40:16.72	+42:56:28.6	10.0, 11.3	10.3	58.4	21.1	1607/30	2.55	Y	
G82.317+0.689	20:40:28.99	+42:55:24.5	10.0, 11.3	10.4	1.74	0.60	1607/30			
G84.193+1.439	20:43:36.36	+44:51:52.1	-2.80, -2.14	-2.38	0.49	0.09	1608/18	2.54	Y	

Name (gl, gb) ($^{\circ}$, $^{\circ}$) (1)	R.A. (J2000) (h m s) (2)	DEC (J2000) ($^{\circ}$ $'$ $''$) (3)	ΔV (km s $^{-1}$) (4)	v_p (km s $^{-1}$) (5)	S_p (Jy) (6)	S_i (Jy km s $^{-1}$) (7)	Epoch yy/mm/dd (8)	Distance kpc (9)	Only one features? (10)	Other name (11)
G84.951-0.691	20:55:32.50	+44:06:10.2	-37.0, -25.0	-36.5	5.35	1.52	1609/05	5.35	N	
G84.984-0.529	20:54:58.33	+44:13:58.3	-39.1, -37.9	-38.5	0.53	0.25	1609/05	5.39	N	
G89.930+1.669	21:04:15.41	+49:24:27.4	-70.6, -69.6	-69.9	0.53	0.18	1608/03	7.93	Y	
G99.070+1.200	21:49:40.65	+55:24:51.8	-67.2, -66.1	-66.6	0.48	0.27	1609/07	6.31	N	
G124.015-0.027	01:00:55.42	+62:49:29.5	-41.0, -39.7	-40.3	1.54	0.71	1608/05	2.62	N	
G149.076+0.397	04:01:36.49	+53:19:41.4	-39.7, -37.9	-38.6	1.75	0.68	1608/14	4.73	N	

Table 3. 192 already detected 6.7 GHz methanol masers.

Name (gl, gb) ($^{\circ}$, $^{\circ}$) (1)	R.A. (J2000) (h m s) (2)	DEC (J2000) ($^{\circ}$ $^{\circ}$ $''$) (3)	ΔV (km s $^{-1}$) (4)	v_p (km s $^{-1}$) (5)	S_p (Jy) (6)	S_i (Jy km s $^{-1}$) (7)	Epoch yy/mm/dd (8)	Distance kpc (9)	Ref. (10)
G20.234+0.085	18:27:39.95	−11:14:32.3	59.7, 77.7	73.2	22.9	14.1	16/07/04	5.21	Parkes
G20.315+0.072	18:27:52.06	−11:10:35.8	71.4, 74.2	73.3	1.05	0.55	16/07/04		
G20.363−0.014	18:28:16.02	−11:10:25.4	49.6, 59.6	56.2	5.05	9.65	16/07/04	3.47	Parkes
G20.762−0.064	18:29:12.19	−10:50:36.0	53.7, 64.0	61.2	2.09	8.58	16/07/04	3.75	Parkes
G20.926−0.050	18:29:27.80	−10:41:28.8	24.7, 30.4	25.9	8.91	15.3	16/07/04	13.94	Parkes

Note. — Column 1: number; Columns 2 - 5: positions (gl, gb, R.A., decl.); Columns 6 - 9: magnitudes in the 4 *WISE* bands; Columns 10 - 11: the *WISE* color. (This table is available in its entirety in machine-readable form.)

Note. — Column 1: source name; Columns 2 - 3: the targeted positions for the TMRT observations; Column 4: the velocity interval of the maser emission; Column 5: the velocity of peak emission; Column 6: the peak flux density; Column 7: the integrated flux density; Column 8: the epoch of observation; Column 9: estimated kinematic distances by using the Galactic rotation model (<http://bessel.vlbi-astrometry.org/bayesian>); Column 10: whether the spectra of the sources only have one feature? Y: yes; N: no; Column 11: name of associated source in Urquhart et al. (2014); Csengeri et al. (2014).

Note. — Column 1: source name; Columns 2 - 3: targeted positions for the TMRT observations; Column 4: velocity interval of the maser emission; Column 5: velocity of the peak emission; Column 6: peak flux density; Column 7: integrated flux density; Column 8: epoch of observation; Column 9: estimated kinematic distance by using the Galactic rotation model (Reid et al. 2009, 2014, <http://bessel.vlbi-astrometry.org/bayesian>); Column 10: the discovery references Parkes (Breen et al. 2015), Szy12 (Szymczak et al. 2012).

Note. — Table 3 is published in its entirety in the electronic edition of the *Astrophysical Journal*. A portion is shown here for guidance regarding its form and content.

Table 4. Comparison between the spectral profiles of our survey and the previous surveys.

Name (1)	Name in the previous surveys (2)	Ref. (3)	Notes (4)
G20.234+0.085	G20.237+0.065/G20.239+0.065	Parkes	Both show strong features at 71.9 km s^{-1} and 73.2 km s^{-1} .
G20.363–0.014	G20.364–0.013	Parkes	Has not changed a lot.
G20.762–0.064	G20.733–0.059	Parkes	With an angular separation of $105.5''$ away from G20.762–0.064, G20.733–0.059 only had one strong feature at 60.7 km s^{-1} .
G20.926–0.050	G20.926–0.050	Parkes	Show similar features at 25.6 km s^{-1} , 25.9 km s^{-1} and 27.4 km s^{-1} .
G21.023–0.063	G21.023–0.063	Parkes	Same features.
G21.370–0.226	21.407–0.254	Szy12	The feature at 95.2 km s^{-1} disappears and a feature rises at 93.0 km s^{-1} in our TMRT survey.
G22.050+0.211	G22.039+0.222	Parkes	With an angular separation of $60.3''$, a new feature at 54.6 km s^{-1} is confirmed.
G22.355+0.066	G22.356+0.066	Parkes	A new feature at 78.8 km s^{-1} .
G23.010–0.410	G23.010–0.410	Parkes	Strong features at similar velocities.
G23.185–0.380	G23.207–0.377	Parkes	A new feature at 82.9 km s^{-1} .
G23.271–0.256	G23.257–0.241	Parkes	Similar features at the same velocities.
G23.389+0.185	G23.389+0.185	Parkes	Similar.
G23.436–0.184	G23.437–0.184/G23.440–0.182	Parkes	Both show features at 96.6 , 97.6 , 98.0 , 102.9 , 104.0 , 107.0 km s^{-1} .
G23.653–0.143	G23.657–0.127	Parkes	Similar features at the same velocity range.
G23.680–0.189	G23.706–0.198	Parkes	The feature at 58.2 km s^{-1} seems obscure in our observation.
G23.899+0.065	G23.885+0.060/G23.901+0.077	Parkes	Share features at 31.6 , 35.7 , 44.0 and 44.9 km s^{-1} , but a new feature at 42.8 km s^{-1} .
G23.965–0.110	G23.966–0.109/G23.986–0.089/G23.996–0.100	Parkes	Share features at 65.1 , 67.7 , 68.2 and 71.0 km s^{-1} .
G24.148–0.009	G24.148–0.009	Parkes	Similar features at the same velocities.
G24.328+0.144	G24.329+0.144	Parkes	Both show features at 110.3 , 111.9 , 112.9 , 115.4 and 119.8 km s^{-1} .
G24.485+0.180	G24.461+0.198	Parkes	The features at the velocity range of 119.9 to 126.0 km s^{-1} are much weaker now.
G24.528+0.337	G24.541+0.312	Parkes	The feature at 106.8 km s^{-1} in our TMRT detection is much weaker.
G24.634–0.323	G24.634–0.324	Parkes	A new feature at 38.0 km s^{-1} .
G24.790+0.084	G24.790+0.083a/G24.790+0.083b	Parkes	Similar features at the same velocities.
G24.943+0.074	G24.920+0.086/G24.943+0.074	Parkes	Similar features but one at 47.7 km s^{-1} is not seen by the TMRT survey.
G25.256–0.446	G25.270–0.4349	Parkes	Both show features at the same velocities.
G25.346–0.189	G25.382–0.182/G25.407–0.170	Parkes	Similar features.
G25.395+0.033	25.39+0.03	Szy12	Only one feature at 95.7 km s^{-1} .
G25.410+0.105	G25.411+0.105	Parkes	A feature at 93.4 km s^{-1} is not seen in our survey.
G25.498+0.069	G25.494+0.062	Parkes	A new weak feature at 92.0 km s^{-1} appeared in our survey.
G25.709+0.044	G25.710+0.044	Parkes	This source has not changed.
G25.613+0.226	G25.613+0.226	Parkes	A feature at 109.8 km s^{-1} seems disappeared in our TMRT survey.
G25.649+1.050	G25.650+1.049	Parkes	This source remains stable.

Table 4—Continued

Name (1)	Name in the previous surveys (2)	Ref. (3)	Notes (4)
G25.837–0.378	G25.838–0.378	Parkes	Both have weak features at the same velocities.
G26.421+1.686	G26.422+1.685	Parkes	A new feature at 30.4 km s^{-1} from our TMRT survey.
G26.545+0.423	G26.545+0.42	Parkes	Only one feature at 82.5 km s^{-1} .
G26.598–0.024	G26.598–0.024	Parkes	This source remains unchanged.
G26.623–0.259	G26.601–0.221	Parkes	Due to the separation of $2.5'$, G26.601–0.221 has many much stronger features.
G26.645+0.021	G26.648+0.018	Parkes	Features at 104.0 , 107.0 , 111.7 and 114.3 km s^{-1} are not shown in our TMRT detection.
G27.220+0.261	G27.220+0.261	Parkes	A weak feature at 6.20 km s^{-1} is not seen in our detection.
G27.222+0.136	G27.221+0.136	Parkes	Share features at a velocity range of 112.0 to 120.8 km s^{-1} , but a feature at 110.2 km s^{-1} seems disappeared in our TMRT detection.
G27.287+0.154	G27.286+0.151	Parkes	G27.286+0.151 has a much larger velocity range of 23.4 to 36.7 km s^{-1} than the velocity range of 34.0 to 36.9 km s^{-1} from our TMRT observation.
G27.725+0.037	G27.757+0.050	Parkes	Share weak features at the same velocity range.
G27.784+0.057	G27.784+0.057	Parkes	Similar.
G27.795–0.277	G27.783–0.259	Parkes	A feature at 93.6 km s^{-1} has disappeared in our TMRT observation.
G28.147–0.004	G28.146–0.005	Parkes	Similar features.
G28.180–0.093	G28.201–0.049	Parkes	Features at 94.5 , 100.2 and 111.9 km s^{-1} have disappeared in our TMRT detection.
G28.287–0.348(Left)	G28.282–0.359	Parkes	Share similar features.
G28.287–0.348(Right)	G28.305–0.387	Parkes	Similar.
G28.320–0.012	G28.321–0.011	Parkes	Both have features at 96.7 , 97.5 , 102.7 and 104.7 km s^{-1} .
G28.393+0.085	G28.397+0.081	Parkes	Similar.
G28.532+0.129	G28.523+0.127/G28.532+0.129	Parkes	Show features at 24.8 , 25.0 and 39.8 km s^{-1} .
G28.609+0.017	G28.608+0.018	Parkes	Our TMRT detection has a new feature at 104.6 km s^{-1} .
G28.832–0.250	G28.832–0.253	Parkes	Our detection has some new features at a velocity range of 99.7 to 103.6 km s^{-1} .
G28.843+0.494	G28.842+0.493	Parkes	Both have features at the same velocities.
G28.862+0.066	G28.861+0.065	Parkes	G28.861+0.065 has a much weaker feature at 105.3 km s^{-1} .
G29.320–0.162	G29.320–0.162	Parkes	A feature at 40.3 km s^{-1} is not detected by the TMRT survey.
G29.835–0.012	G29.863–0.044	Parkes	Our TMRT detection shows new features at 93.8 , 96.0 and 99.6 km s^{-1} .
G29.927+0.054	G29.955–0.016	Parkes	The feature at 100.2 km s^{-1} in the spectrum of G29.955–0.016 disappeared in the TMRT survey.
G29.941–0.070	G29.978–0.047	Parkes	Similar features.
G30.004–0.265	G29.993–0.282/G30.010–0.273	Parkes	Both have two features at the same velocities.
G30.250–0.232	30.30–0.20	Szy12	The profile of our TMRT detection is much more complex with a wider velocity range.
G30.370+0.483	G30.370+0.482	Parkes	Both have features at 12.3 , 16.7 and 19.4 km s^{-1} .
G30.403–0.297	G30.400–0.296	Parkes	Similar features but one at 105.0 km s^{-1} has become stronger.

Table 4—Continued

Name (1)	Name in the previous surveys (2)	Ref. (3)	Notes (4)
G30.419–0.232	G30.419–0.232	Parkes	A feature at 111.2 km s^{-1} disappears now.
G30.536–0.004	G30.542+0.011	Parkes	Similar features at the same velocity range.
G30.589–0.043	G30.589–0.043	Parkes	Share similar features.
G30.662–0.139	G30.703–0.068	Parkes	The feature at 86.0 km s^{-1} is not seen by the TMRT survey.
G30.807+0.080	G30.774+0.078	Parkes	Share features at the same velocity range.
G30.770–0.804	G30.771–0.804	Parkes	Similar.
G30.789+0.232(Left)	G30.780+0.230	Parkes	They share the same spectral profiles.
G30.788+0.203(Right)	G30.788+0.204	Parkes	Share similar features at the same velocity range.
G30.810–0.050	G30.822–0.053/G30.818–0.057	Parkes	The features at 91.3 and 103.4 km s^{-1} are difficult to find in the TMRT survey.
G30.819+0.273	G30.818+0.273	Parkes	Both have features at 100.5 , 101.1 , 102.4 , 104.8 and 110.2 km s^{-1} .
G30.866+0.114	G30.851+0.123	Parkes	Show similar profile but the feature at 37.2 km s^{-1} is difficult to distinguish now.
G30.823+0.134(Right)	G30.788+0.204	Parkes	Similar features.
G30.897+0.163	G30.898+0.161	Parkes	This source has not changed.
G30.959+0.086	G30.960+0.086	Parkes	A feature at 36.0 km s^{-1} seems gone now.
G30.972–0.141	G30.972–0.142	Parkes	Similar features within a velocity range of 73.6 to 80.6 km s^{-1} .
G30.973+0.562	G30.973+0.562	Parkes	Only one feature at 20.0 km s^{-1} .
G30.980+0.216	G30.980+0.216	Parkes	The feature at 110.0 km s^{-1} has become much weaker.
G31.076+0.458	G31.076+0.457	Parkes	One feature at 26.6 km s^{-1} seems disappeared now.
G31.159+0.058	G31.158+0.046	Parkes	Similar features at the same velocity range.
G31.237+0.067	G31.281+0.061	Parkes	G31.281+0.061 has similar features with much stronger flux density.
G31.413+0.308	G31.412+0.307	Parkes	The feature at 105.7 km s^{-1} seems obscure now.
G31.579+0.076	G31.581+0.077	Parkes	Similar features at the same velocity range.
G32.045+0.059	G32.045+0.059	Parkes	Almost the same spectral profile.
G32.118+0.090	G32.082+0.078	Parkes	A feature rises at 104.2 km s^{-1} from our TMRT survey.
G32.773–0.059	G32.744–0.057	Parkes	G32.744–0.057 does not have feature at 35.0 km s^{-1} .
G32.798+0.190	G32.802+0.1931	Parkes	Similar.
G32.828–0.315	G32.825–0.328	Parkes	The feature at 84.0 km s^{-1} in G32.825–0.328 cannot be seen in the TMRT survey.
G32.992+0.034	G32.992+0.03	Parkes	Almost the same features at the same velocity range.
G33.143–0.088(Left)	G33.133–0.092	Parkes	Similar features.
G33.092–0.073(Right)	G33.093–0.073	Parkes	The features at 95.7 , 98.3 and 106.0 km s^{-1} in the spectrum of G33.093–0.073 have become much weaker now.
G33.322–0.364	G33.317–0.360	Parkes	The feature at 30.9 km s^{-1} seems disappear now.
G33.393+0.010	G33.393+0.010	Parkes	A new feature at 107.5 km s^{-1} .
G33.638–0.035	G33.634–0.021	Parkes	One weak peak at 102.9 km s^{-1} .

Table 4—Continued

Name (1)	Name in the previous surveys (2)	Ref. (3)	Notes (4)
G33.641–0.228	G33.641–0.228	Parkes	Has features at 58.8, 59.6, 60.3, 61.8, 62.7 and 63.2 km s ^{−1} .
G33.726–0.119	G33.725–0.120	Parkes	A weak feature at 57.4 km s ^{−1} is not seen in our TMRT survey.
G34.096+0.018	G34.096+0.018	Parkes	Features at 54.9 and 57.3 km s ^{−1} are weaker now.
G34.229+0.133	G34.244+0.133	Parkes	There are new features at 52.1 and 62.7 km s ^{−1} .
G34.411+0.235	G34.396+0.222	Parkes	Similar features.
G34.789–1.392	G34.791–1.387	Parkes	Share features at 44.1, 45.0, 46.3 and 47.2 km s ^{−1} .
G34.757+0.025	G34.82+0.35	Parkes	The only one feature at 76.6 km s ^{−1} is stronger now.
G34.974+0.365	G35.025+0.350	Parkes	The spectrum of G35.025+0.350 has much stronger and more complex features at a wider velocity range of 41.1 to 47.0 km s ^{−1} .
G35.141–0.750	G35.132–0.744	Parkes	The peak feature at 35.4 km s ^{−1} has nearly disappeared now.
G35.194–1.725	G35.200–1.736	Parkes	Both spectra show similar features at a velocity range of 39.9 to 45.7 km s ^{−1} .
G35.197–0.729	G35.197–0.743/G35.197–0.743n	Parkes	Similar features.
G35.247–0.237	G35.247–0.237	Parkes	A weak feature at 72.9 km s ^{−1} seems disappear now.
G35.398+0.025	G35.397+0.025	Parkes	The feature at 90.3 km s ^{−1} in our TMRT detection is new.
G35.578+0.048	G35.588+0.060	Parkes	The feature at 52.0 km s ^{−1} has disappeared.
G35.792–0.174	G35.793–0.175	Parkes	Same features at a velocity range of 58.5 to 63.1 km s ^{−1} .
G36.137+0.564	G36.115+0.552	Parkes	Both surveys show features at 70.4, 71.8, 72.8, 74.7, 75.8, 81.6, 82.2 and 84.0 km s ^{−1} .
G36.634–0.203	G36.634–0.203	Parkes	Share the only one feature at 77.4 km s ^{−1} .
G36.705+0.096	G36.705+0.096	Parkes	The spectrum at a velocity range of 51.9 to 55.9 km s ^{−1} has less features now but is much more complex at a velocity range of 61.2 to 63.9 km s ^{−1} .
G36.833–0.031	G36.839–0.022	Parkes	Both spectra have features at 54.7, 55.4, 57.0, 61.2, 62.0 and 63.6 km s ^{−1} .
G36.919+0.483	G36.918+0.483	Parkes	One feature at the same velocity with a similar flux density.
G37.043–0.035	G37.030–0.038/G37.043–0.035	Parkes	Both spectra show features at 78.4, 80.0, 80.8, 83.7 and 84.8 km s ^{−1} .
G37.430+1.517	G37.430+1.518	Parkes	Both surveys show features at the same velocity range.
G37.479–0.105	G37.546–0.112	Parkes	Both surveys find features at 50.1 and 52.6 km s ^{−1} .
G37.554+0.201	G37.554+0.201	Parkes	The feature at 84.9 km s ^{−1} has grown stronger than the feature at 83.7 km s ^{−1} now.
G37.602+0.428	G37.598+0.425	Parkes	The feature at 85.8 km s ^{−1} is slightly weak now.
G37.763–0.215	G37.763–0.215	Parkes	Similar features at the same velocity range of 54.1 to 70.0 km s ^{−1} .
G38.076–0.265	38.038–0.300	Szy12	Both spectra show features at 55.8 and 57.2 km s ^{−1} .
G38.119–0.229	G38.119–0.229	Parkes	The features at 77.3 and 79.2 km s ^{−1} have become weak after comparing with the strongest feature.
G38.202–0.068	G38.203–0.067	Parkes	Almost the same profile at the same velocity range of 77.8 to 85.1 km s ^{−1} .
G38.255–0.200	G38.255–0.200	Parkes	Both have several weak features at the same velocity range.
G38.258–0.074	G38.258–0.074	Parkes	Share features at 7.09, 12.3 and 15.5 km s ^{−1} .

Table 4—Continued

Name (1)	Name in the previous surveys (2)	Ref. (3)	Notes (4)
G38.598–0.213	G38.598–0.212	Parkes	The feature at 69.2 km s^{-1} seems to have disappeared now.
G38.933–0.361	G38.916–0.353	Parkes	The peak feature at the same velocity range is weaker now.
G39.100+0.491	G39.100+0.491	Parkes	Both surveys detect features at 14.6 , 15.8 , 17.7 , 24.8 and 28.7 km s^{-1} , but the feature at 14.6 km s^{-1} is much weaker now.
G39.387–0.141	G39.388–0.141	Parkes	Our TMRT detection shows a new feature at 72.0 km s^{-1} .
G40.282–0.220	G40.282–0.219	Parkes	The spectrum of G40.282–0.219 has much more and stronger features with a much larger velocity range.
G40.425+0.700	G40.425+0.700	Parkes	Same spectral profile.
G40.597–0.719	G40.597–0.719	Parkes	Similar.
G40.622–0.138	G40.622–0.138	Parkes	Both surveys show features at 30.2 , 31.3 , 31.9 and 36.3 km s^{-1} .
G40.964–0.025	G40.934–0.041	Parkes	Both have three features at 36.9 , 37.5 and 41.1 km s^{-1} .
G41.121–0.107	G41.121–0.107	Parkes	The feature at 36.6 km s^{-1} is weaker and the feature at 37.2 km s^{-1} is stronger now.
G41.307–0.169	G41.348–0.136	Parkes	Features at a velocity range of 6.8 to 9.4 km s^{-1} are not seen now.
G42.035+0.191	G42.034+0.190	Parkes	Similar profile.
G42.692–0.129	G42.698–0.147	Parkes	Similar spectral profile but our TMRT detection is much weaker.
G43.037–0.453	G43.038–0.453	Parkes	Unchanged.
G43.076–0.078	G43.074–0.077	Parkes	Almost the same profile at the same velocity range of 9.70 to 11.3 km s^{-1} .
G43.148+0.013	G43.149+0.013/G43.165+0.013/G43.167–0.004 /G43.171+0.005/G43.175–0.015	Parkes	Similar features in a quite large velocity range.
G43.178–0.519	G43.180–0.518	Parkes	Five features at 55.8 , 58.1 , 58.9 , 59.5 and 65.1 km s^{-1} .
G43.808–0.080	G43.795–0.127	Parkes	Almost same.
G43.890–0.790	G43.890–0.784	Parkes	One feature at 56.6 km s^{-1} becomes stronger and the feature at 49.7 km s^{-1} is no longer there now.
G45.070+0.124	G45.071+0.132	Parkes	A new feature at 59.8 km s^{-1} .
G45.360–0.598	G45.380–0.594	Parkes	Only one feature at the same velocity.
G45.454+0.060	G45.445+0.069/G45.467+0.053	Parkes	The feature at 49.8 km s^{-1} seems weaker.
G45.493+0.126	G45.493+0.126/G45.473+0.134	Parkes	The feature at 73.2 km s^{-1} has disappeared now.
G45.804–0.356	G45.804–0.356	Parkes	Similar features at the same velocity range.
G48.905–0.261	G48.902–0.273	Parkes	G48.905–0.261 has three weak features at 72.2 , 74.3 and 75.2 km s^{-1} , while G48.902–0.273 only has one feature at 71.8 km s^{-1} .
G48.991–0.299	G48.990–0.299	Parkes	Only one feature at 71.6 km s^{-1} .
G49.043–1.079	G49.043–1.079	Parkes	The spectral profile has changed.
G49.265+0.311	G49.265+0.311	Parkes	The weak feature at -6.66 km s^{-1} has become a little stronger.
G49.466–0.408	G49.482–0.402/G49.489–0.369/G49.490–.388	Parkes	Our TMRT observation shows a new feature at 61.0 km s^{-1} .
G49.599–0.249	G49.599–0.249	Parkes	The feature at 66.7 km s^{-1} has become stronger and the peak feature at 63.1 km s^{-1} in the MMB survey is much weaker.

Table 4—Continued

Name (1)	Name in the previous surveys (2)	Ref. (3)	Notes (4)
G50.034+0.581	G50.035+0.582	Parkes	The feature at a velocity range of -11.2 to -8.25 km s $^{-1}$ has become much weaker.
G50.779+0.152	G50.779+0.152	Parkes	Similar features at the same velocity range of 48.1 to 50.8 km s $^{-1}$.
G51.678+0.719	G51.679+0.719	Parkes	The features at -3.89 and 2.00 km s $^{-1}$ seems have disappeared now.
G52.199+0.723	G52.199+0.723	Parkes	Similar features at a velocity range of 2.28 to 4.52 km s $^{-1}$.
G52.663–1.092	G52.663–1.092	Parkes	Both surveys detected features at 56.3 , 65.2 , 65.9 and 66.4 km s $^{-1}$.
G52.922+0.414	G52.922+0.414	Parkes	Similar features.
G53.022+0.100	G53.036+0.113	Parkes	Only one feature at 10.0 km s $^{-1}$.
G53.141+0.071	G53.142+0.071	Parkes	Similar profile at a velocity range of 23.7 to 24.8 km s $^{-1}$.
G53.618+0.036	G53.618+0.035	Parkes	G53.618+0.035 has almost the same but much stronger features.
G56.963–0.234	G56.963–0.235	Parkes	Both have only one feature at 29.7 km s $^{-1}$.
G58.775+0.647	G58.775+0.644	Parkes	A new feature at 36.6 km s $^{-1}$.
G59.634–0.192	G59.634–0.192	Parkes	The features at 23.3 and 25.9 km s $^{-1}$ are new.
G59.785+0.068	G59.783+0.065	Parkes	Obviously the feature at 19.1 km s $^{-1}$ has become much stronger now.
G59.833+0.672	G59.833+0.672	Parkes	This source remains the same profile.
G69.543–0.973	69.540–0.976/ON1	Szy12	Their spectra show the same profile with features at -0.06 , 1.13 and 14.6 km s $^{-1}$.
G71.522–0.385	71.52–0.38	Szy12	The feature at 10.2 km s $^{-1}$ seems much stronger.
G73.063+1.796	73.06+1.80	Szy12	The feature at -2.54 km s $^{-1}$ becomes brighter and there is a new weak feature at 0.34 km s $^{-1}$.
G75.770+0.344	75.78+0.34	Szy12	The features at -9.53 and -0.95 km s $^{-1}$ are not seen in our TMRT survey.
G78.882+0.723	78.89+0.71	Szy12	One single feature at the same velocity range of -7.41 to -6.51 km s $^{-1}$.
G79.736+0.991	79.736+0.991	Szy12	Similar features at the same velocity range of -6.63 to -2.84 km s $^{-1}$.
G80.862+0.383	80.861+0.383/DR20	Szy12	Two new features at -11.2 and -2.02 km s $^{-1}$.
G81.752+0.591	81.76+0.59/W75S	Szy12	Similar features.
G81.871+0.779	81.87+0.78/W75N	Szy12	Almost the same profile.
G85.394–0.023	85.41+0.00	Szy12	Features at the same velocity range of -33.5 to -27.8 km s $^{-1}$.
G90.921+1.487	90.92+1.49	Szy12	Features at -71.2 , -70.4 and -69.2 km s $^{-1}$ are detected.
G94.609–1.790	94.602–1.796	Szy12	Similar features at the same velocity range.
G98.036+1.446	98.04+1.45	Szy12	Only one feature at the same velocity.
G108.758–0.986	108.76–0.99	Szy12	Both show features at -56.0 , -54.6 , -47.3 and -45.6 km s $^{-1}$.
G111.256–0.770	111.26–0.77	Szy12	Both have four features at -41.2 , -38.7 , -37.8 and, -36.9 km s $^{-1}$.
G111.532+0.759	111.542+0.777/NGC7538	Szy12	They all have similar profile at the same velocity range.
G121.329+0.639	121.298+0.659/L1287	Szy12	The feature at -27.0 km s $^{-1}$ seems obscure now.
G134.029+1.072	133.947+1.064/W3(OH)	Szy12	Both detect this source at a velocity range of -48.5 to -41.6 km s $^{-1}$.
G136.859+1.165	136.84+1.15	Szy12	Only one feature at the same velocity range.

Table 4—Continued

Name (1)	Name in the previous surveys (2)	Ref. (3)	Notes (4)
G174.205–0.069	174.201–0.071/AFGL5142	Szy12	The feature at 0.36 km s^{-1} disappears in our TMRT survey.
G183.349–0.575	183.35–0.58	Szy12	Both spectra show features at -15.2 , -14.5 and, -4.74 km s^{-1} .

Note. — Column 1: source name in our survey; Columns 2: source name in the previous detected surveys; Column 3: the discovery references Parkes (Breen et al. 2015), Szy12 (Szymczak et al. 2012); Column 4: notes about the comparison between the spectral profiles of our survey and the previous surveys.

Table 5: The OTF observations.

Name	OTF Parameters			Epoch yy/mm/dd	Properties of the Fitting Centers			Associated MMB source	Difference
	R.A. (J2000) (h m s)	Decl. (J2000) (° ′ ″)	Side Length (′)		Velocity ranges km s ^{−1}	R.A. (J2000) (h m s)	Decl. (J2000) (° ′ ″)		
(1)	(2)	(3)	(4)	(5)	(6)	(7)	(8)	(9)	(10)
G28.287−0.348	18:44:11.48	−04:17:47.1	10	17/11/21	40.7, 43.1 79.4, 94.2	18:44:13.15 18:44:22.08	−04:18:00.3 −04:17:42.9	G28.282−0.359 G28.305−0.387	4.9 4.7
G30.788+0.203	18:46:48.14	−01:49:24.4	10	17/11/21	47.3, 49.4 75.0, 90.2	18:46:41.34 18:46:48.14	−01:48:34.2 −01:48:54.3	G30.780+0.230 G30.788+0.204	3.9 0.8
G30.823+0.134	18:47:06.88	−01:47:57.9	15	18/01/08	27.0, 29.4 75.4, 90.3	18:47:12.35 18:46:47.68	−01:47:48.8 −01:48:57.7	G30.851+0.123 G30.788+0.204	2.6 1.0
G31.221+0.020	18:48:24.70	−01:28:49.1	20	18/01/08	40.6, 41.8 79.0, 80.3	18:48:01.57 18:48:16.23	−01:33:46.3 −01:31:16.2		
G33.143−0.088	18:52:09.17	+00:08:33.0	10	17/11/29	102.3, 113.2 70.4, 81.8 94.1, 107.2	18:48:12.23 18:52:07.88 18:51:58.54	−01:26:46.0 +00:08:24.0 +00:06:33.9	G31.281+0.061 G33.133−0.092 G33.093−0.073	15.4 11.2 15.0

Table 6: A 6.7 GHz CH₃OH maser sources catalog.

Number	Name (gl, gb) (^o , ^o)	R.A. (J2000) (h m s)	Decl. (J2000) (^o ['] ^{''})	ΔV (km s ⁻¹)	v_p (km s ⁻¹)	S_p (Jy)	Ref.
(1)	(2)	(3)	(4)	(5)	(6)	(7)	(8)
1	0.092-0.663	17 48 25.90	-29 12 05.9	10, 25	23.5	24.8	MMB
2	0.167-0.446	17 47 45.46	-29 01 29.3	9.5, 17	13.8	4.44	MMB
3	0.212-0.001	17 46 07.63	-28 45 20.9	41, 50.5	49.3	3.47	MMB
4	0.315-0.201	17 47 09.13	-28 46 15.7	14, 27	19.4	72.16	MMB
5	0.316-0.201	17 47 09.33	-28 46 16.0	20, 22	21	0.6	MMB
6	0.376+0.040	17 46 21.41	-28 35 40.0	35, 40	37	2.32	MMB
7	0.39-0.03	17 46 41.120	-28 37 05.50	22, 31	28.7	5.8	P05
8	0.409-0.504	17 48 33.48	-28 50 52.5	24.5, 27	25.3	2.77	MMB
9	0.475-0.010	17 46 47.07	-28 32 06.9	23, 31	28.8	3.43	MMB
10	0.496+0.188	17 46 03.96	-28 24 52.8	-12, 2	0.8	32.14	MMB
						

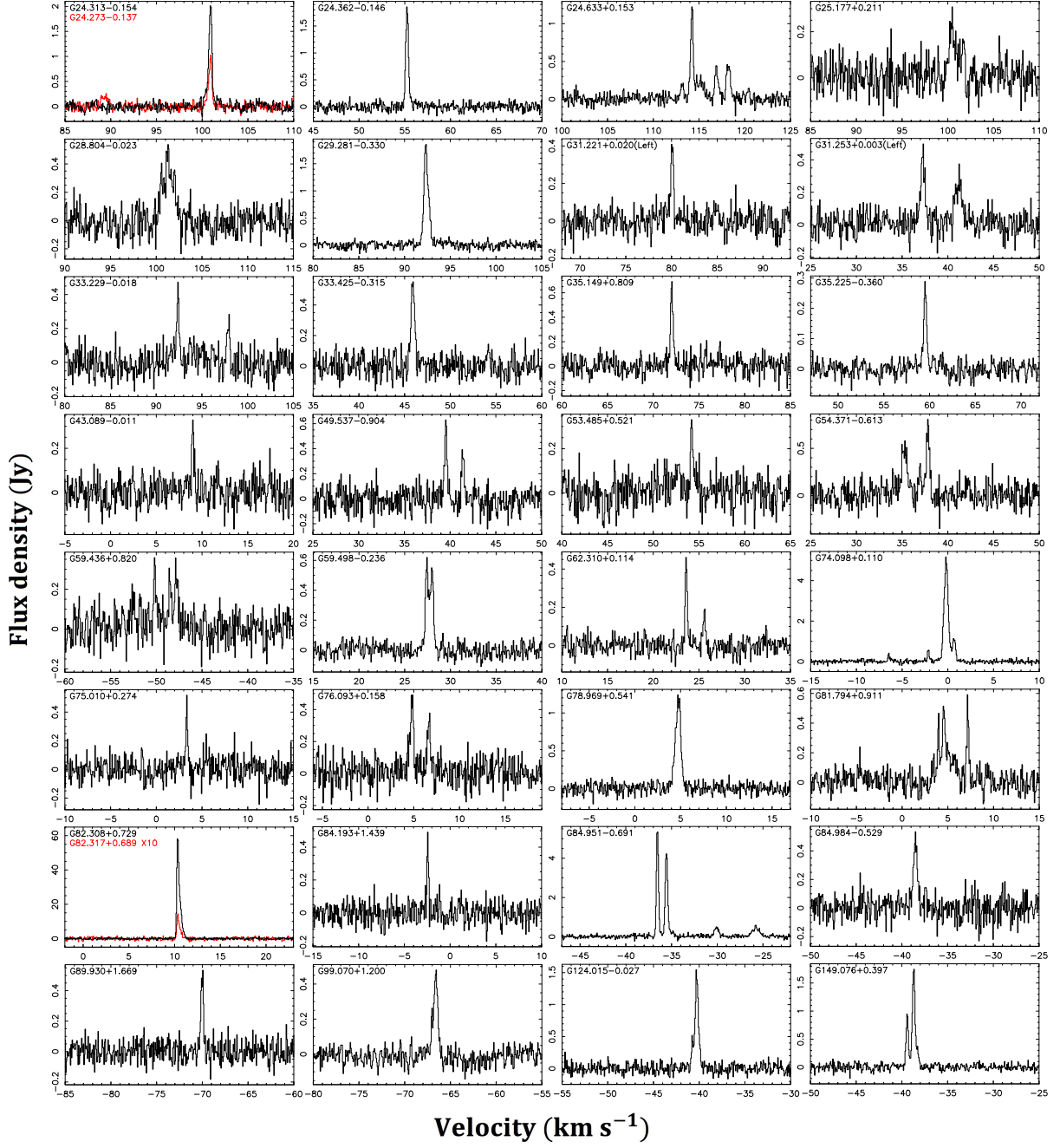


Fig. 1.— The spectrum of the 32 newly detected CH₃OH maser sources by the TMRT. For the same source but detected at two different positions (G24.313–0.154 and G24.273–0.137), we show their spectra in different colors.

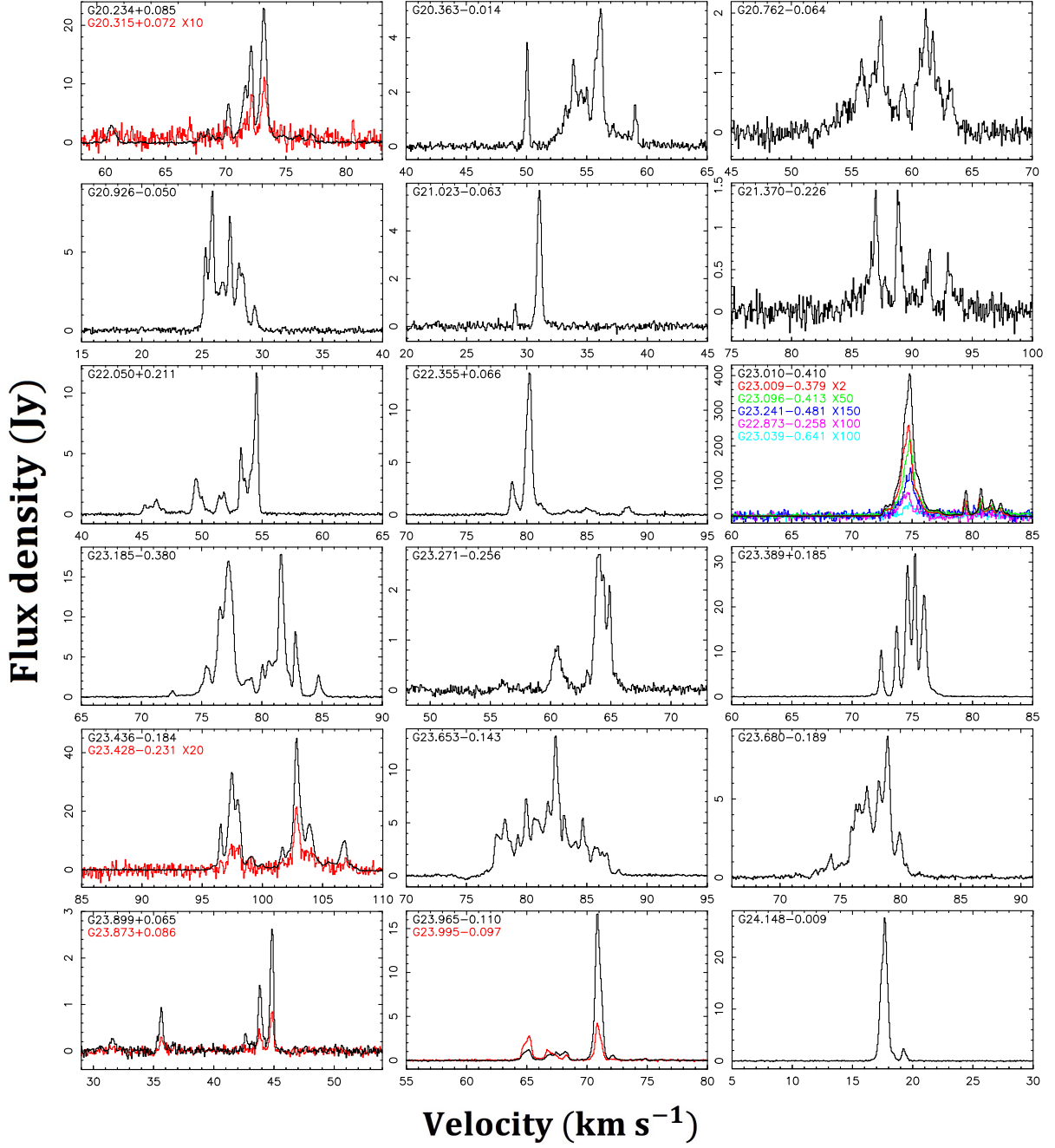


Fig. 2.— The TMRT spectrum of 6.7 GHz CH₃OH maser towards 192 sources which have been previously CH₃OH maser detected. For the same sources but detected at two or more separated positions, we show their spectra in different colors.

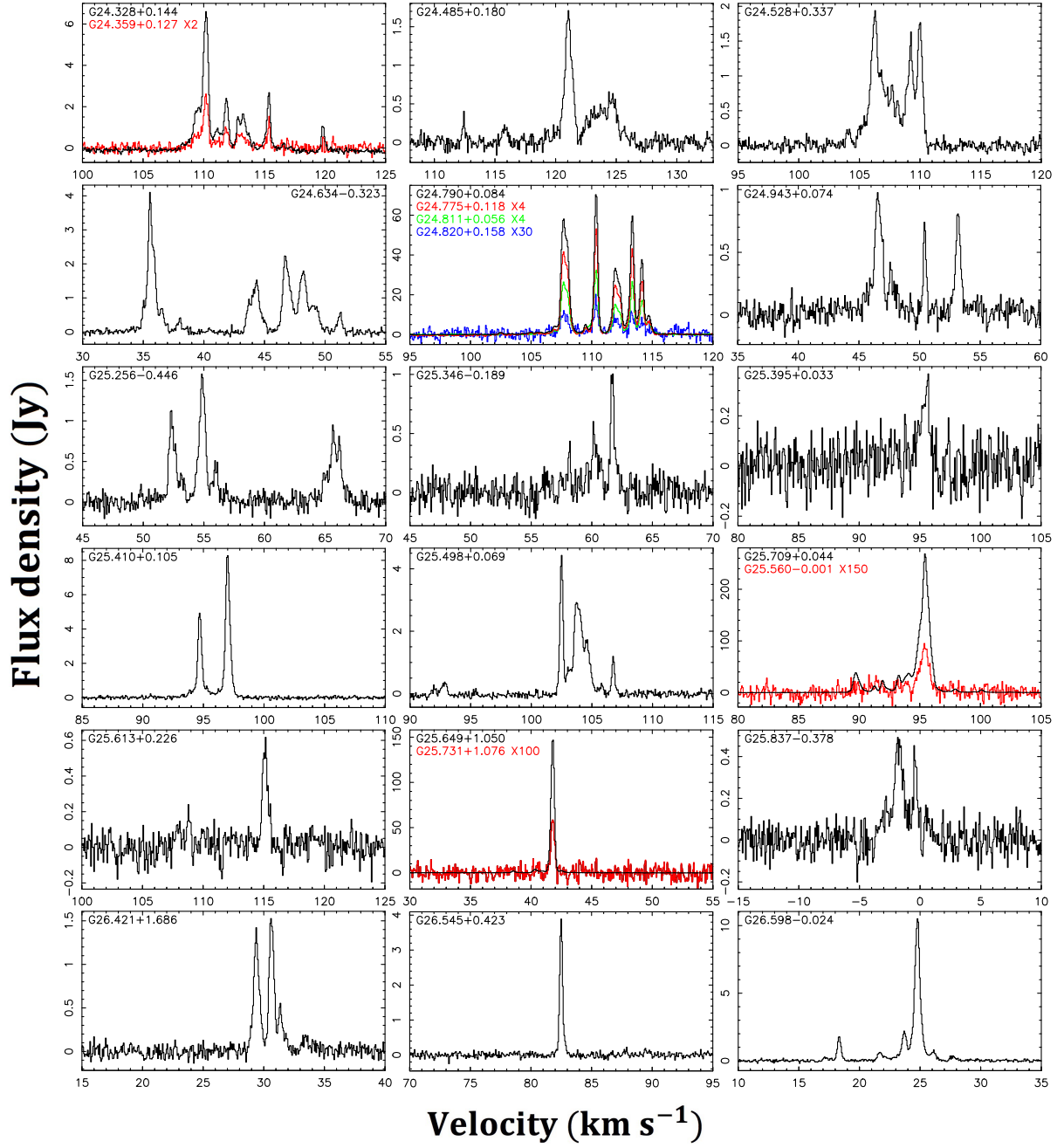


Fig. 2.— Continued

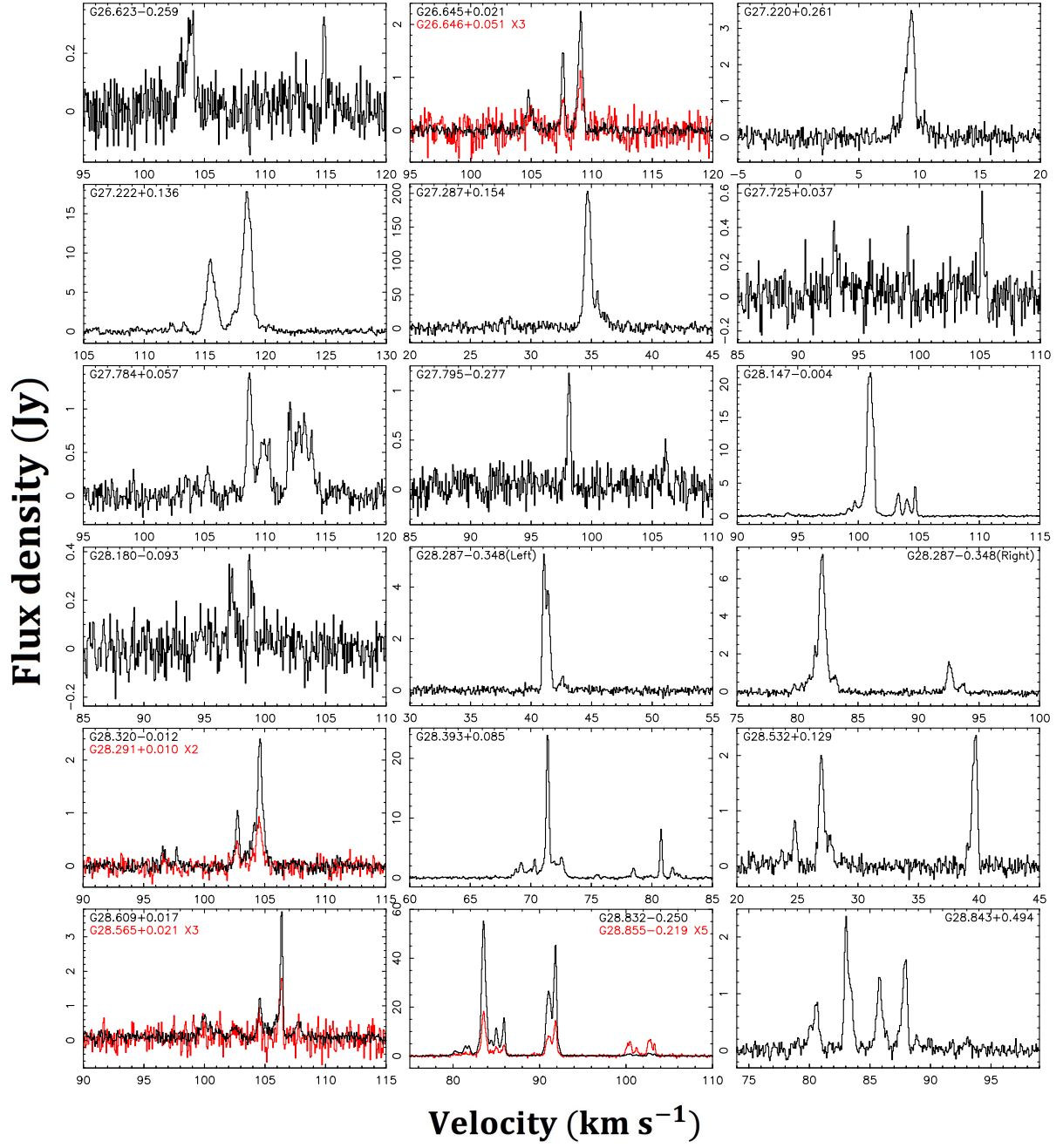


Fig. 2.— Continued

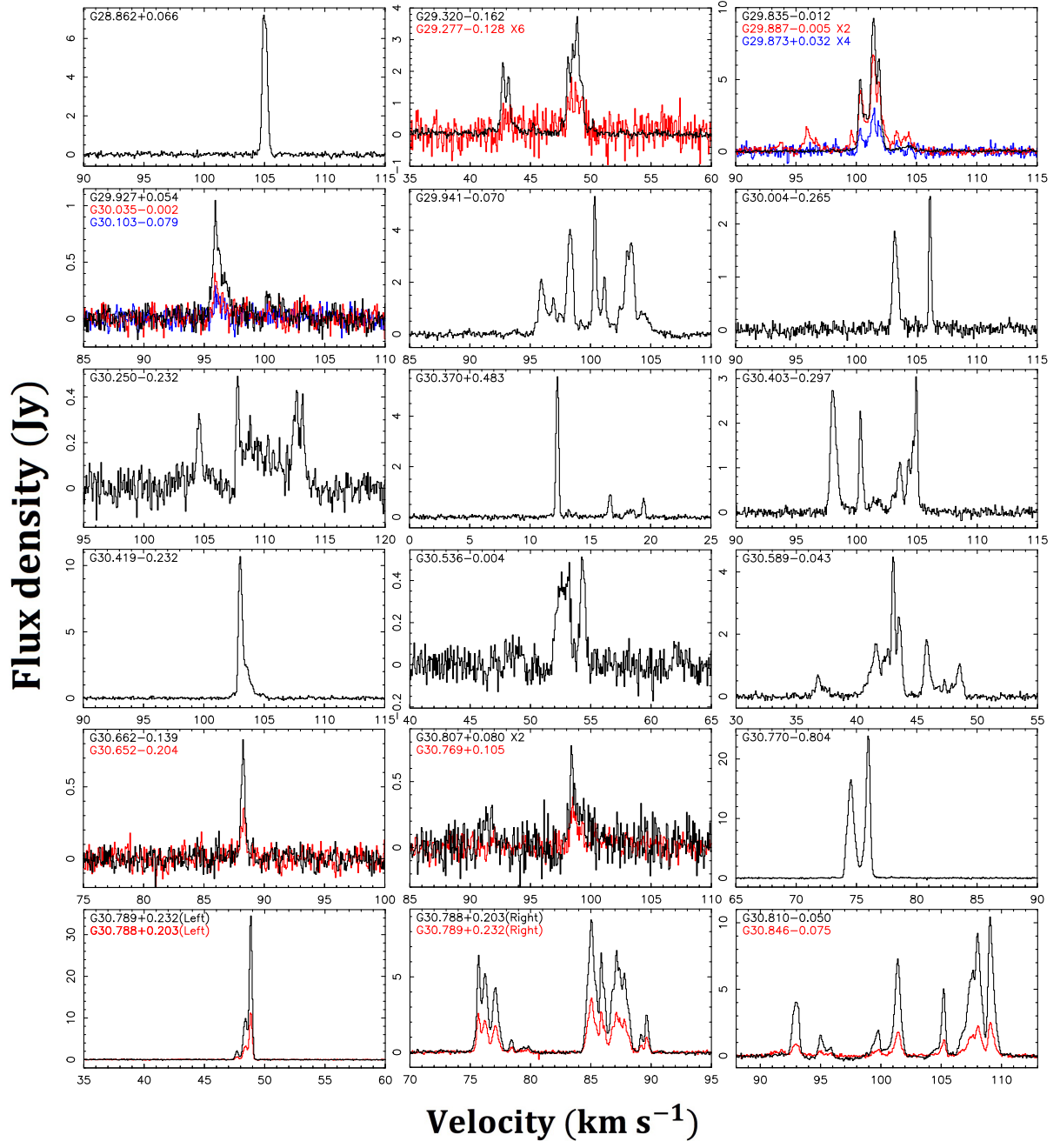


Fig. 2.— Continued

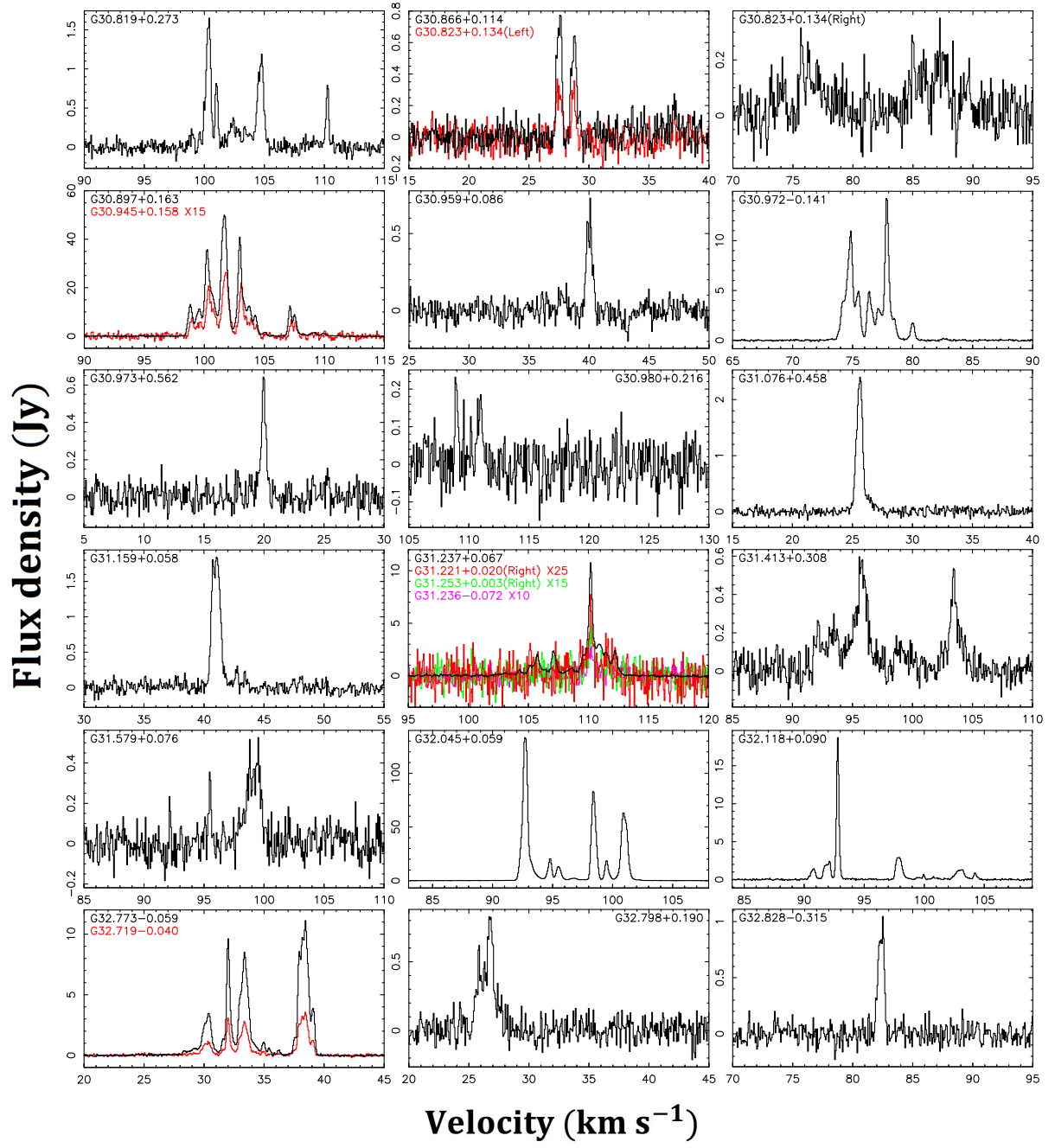


Fig. 2.— Continued

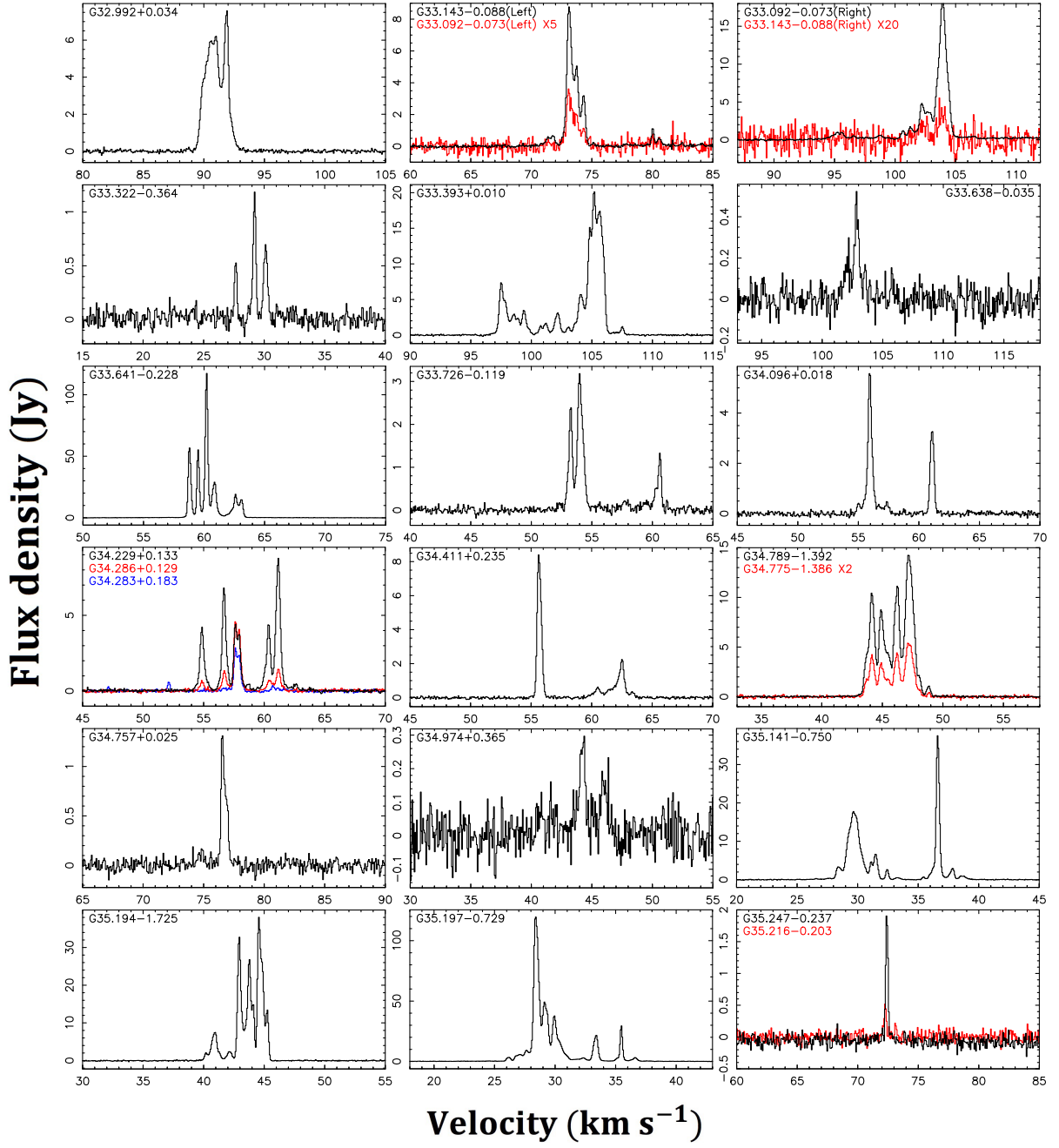


Fig. 2.— Continued

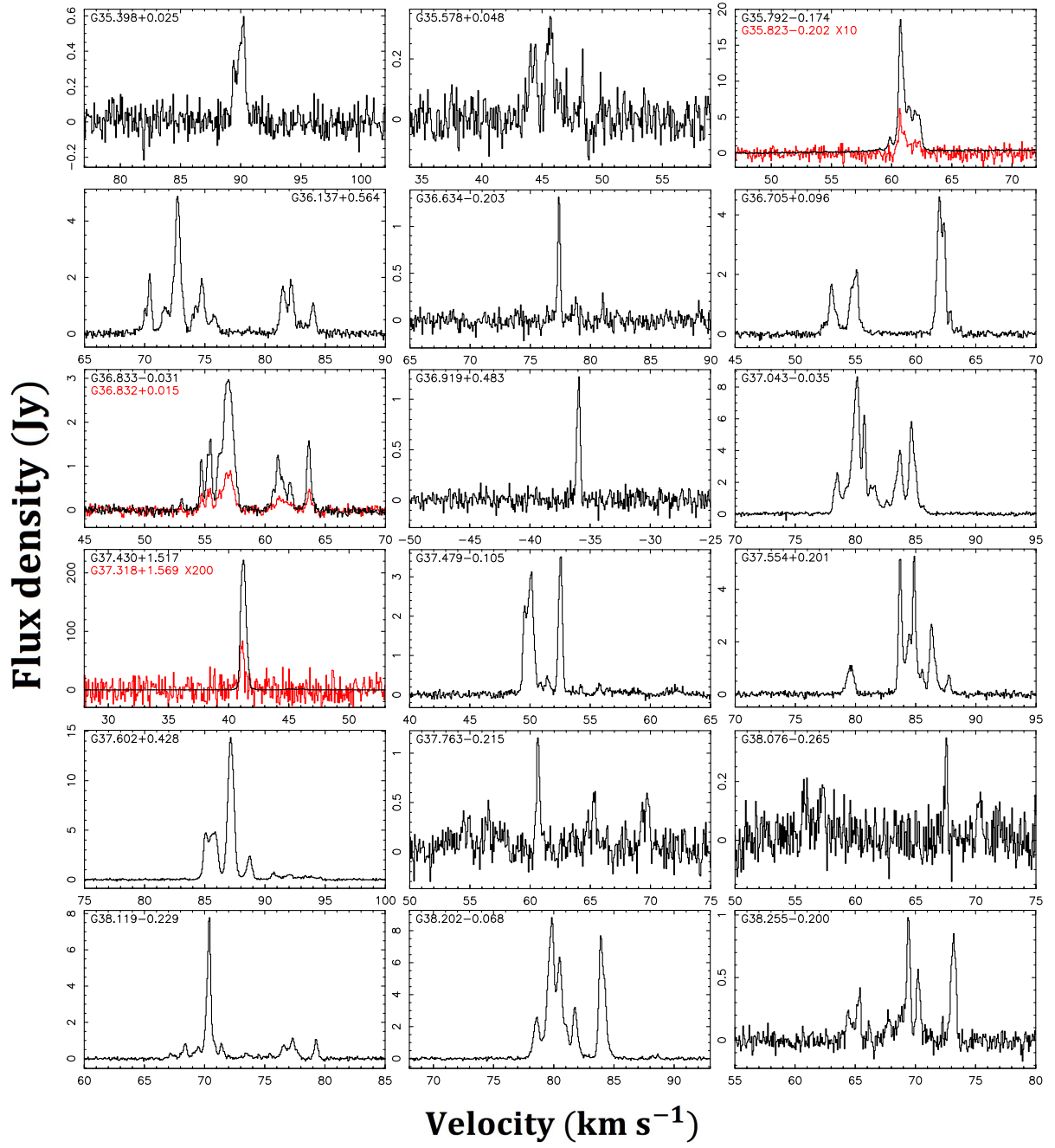


Fig. 2.— Continued

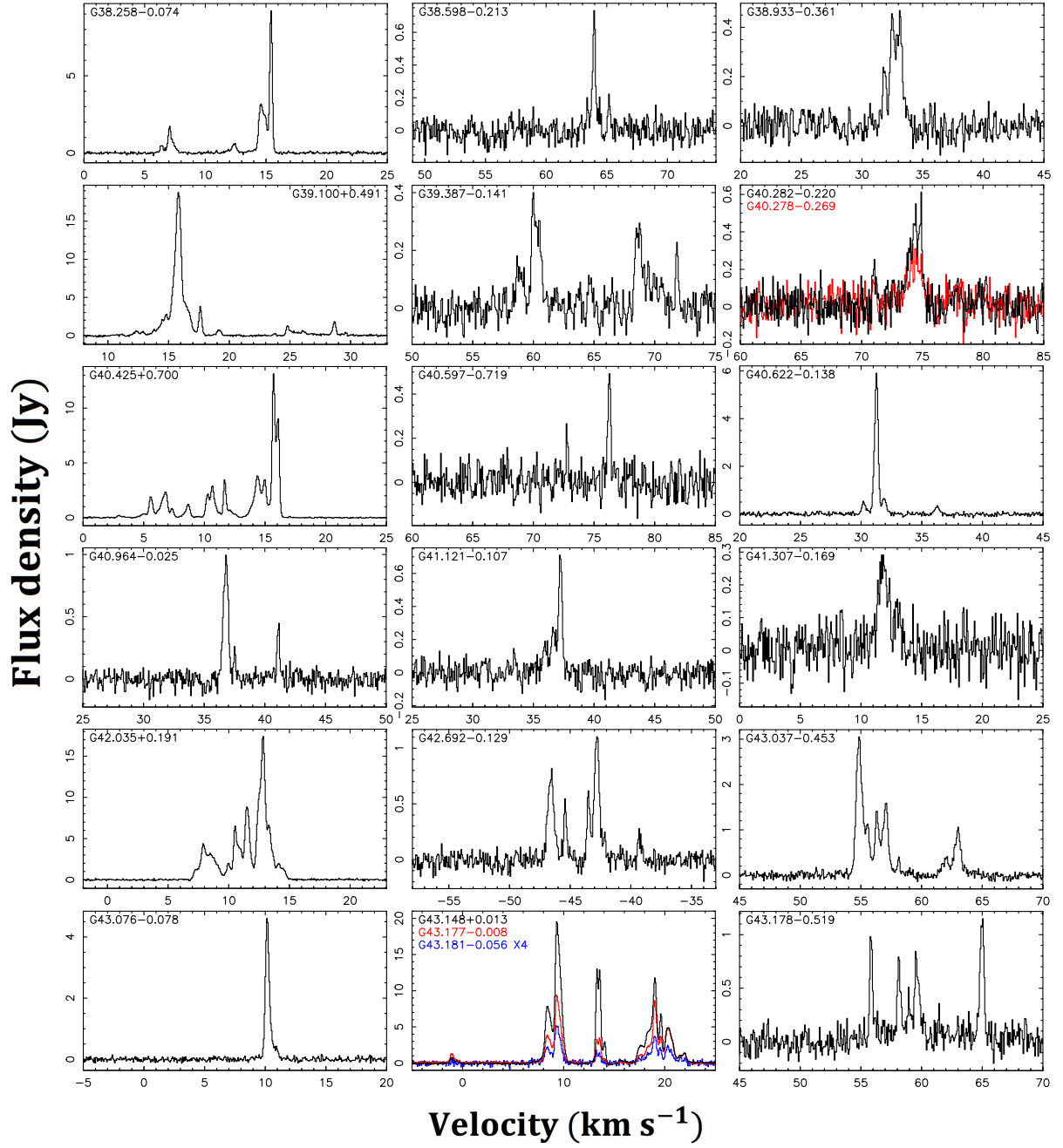


Fig. 2.— Continued

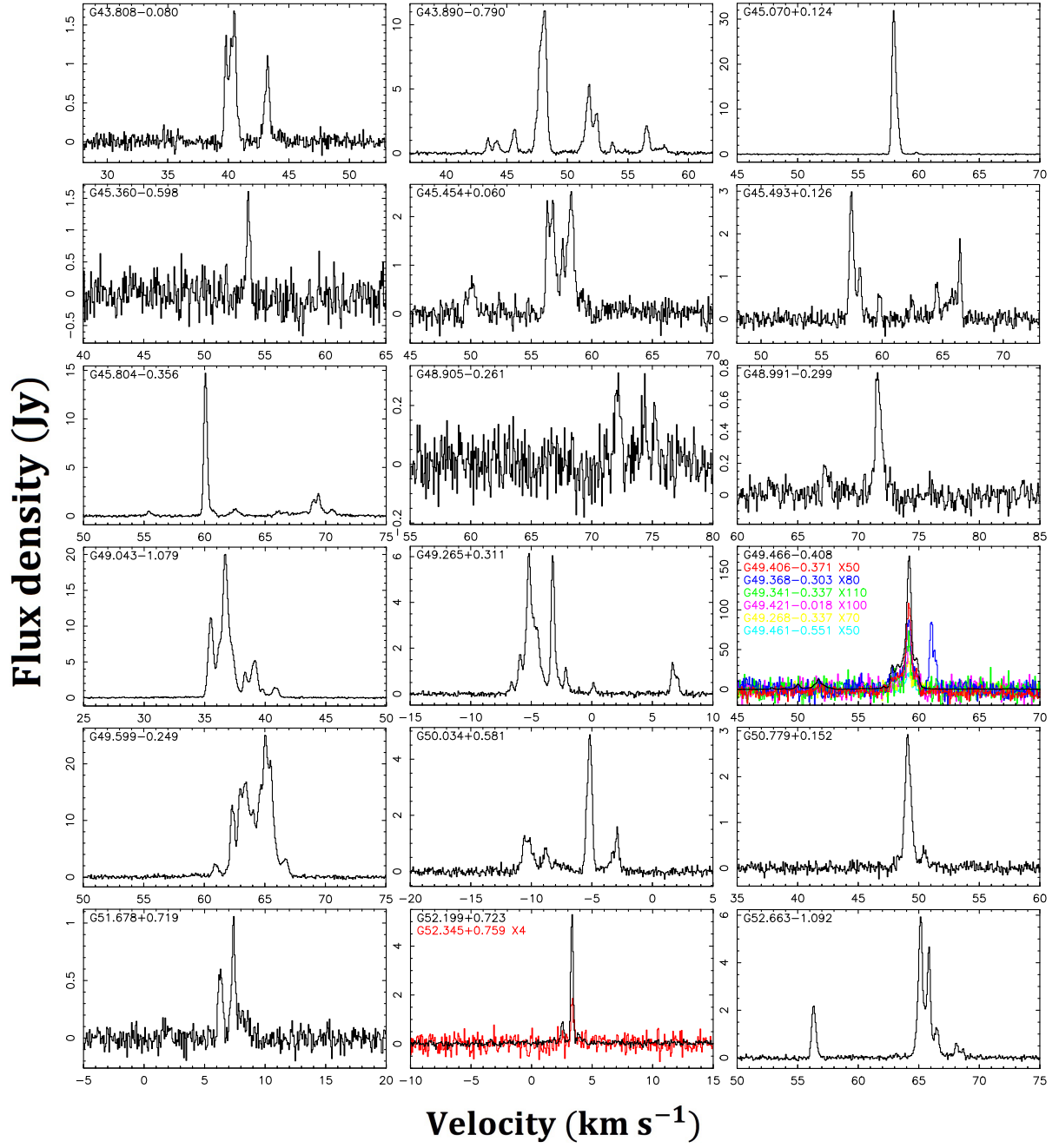


Fig. 2.— Continued

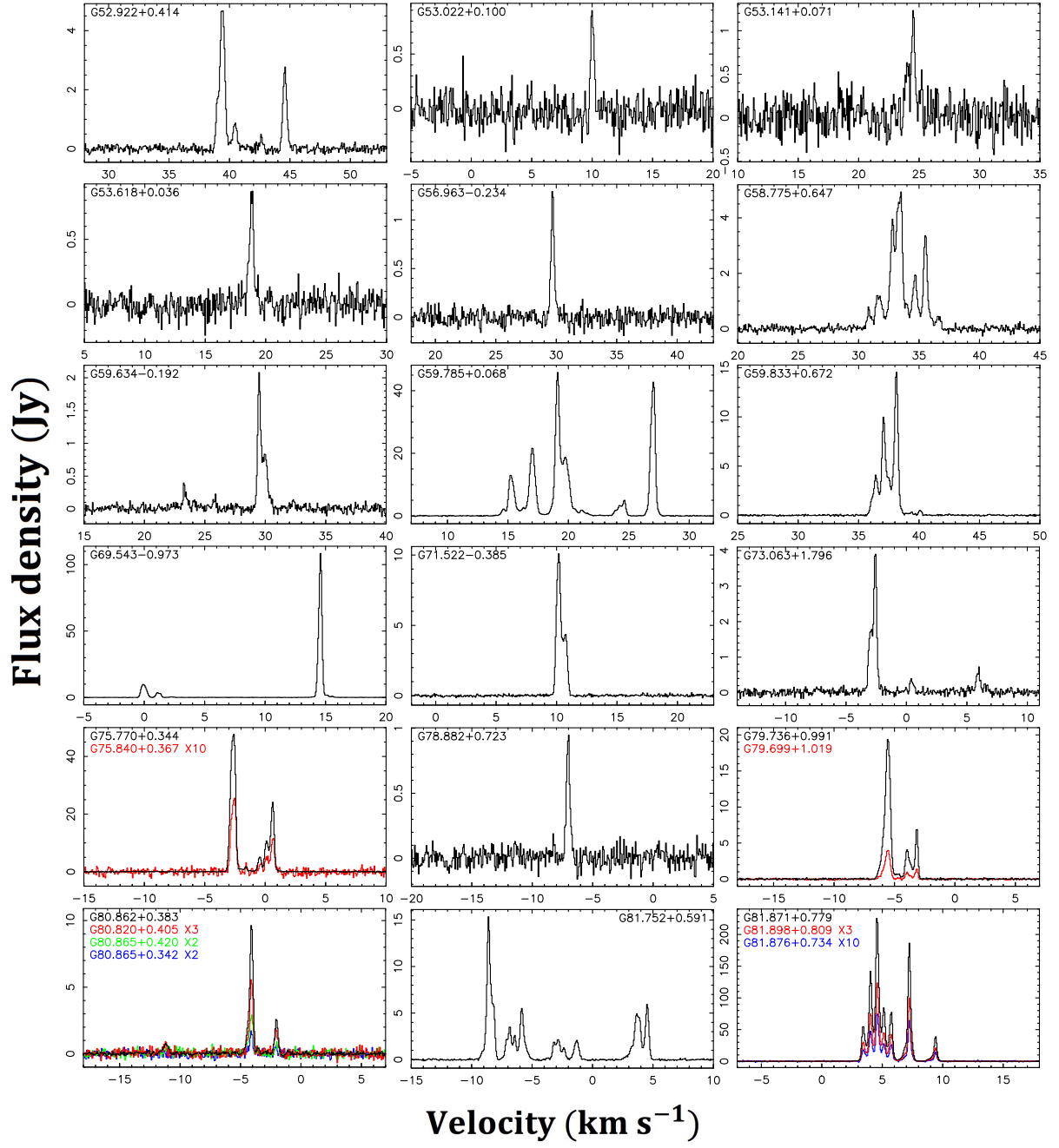


Fig. 2.— Continued

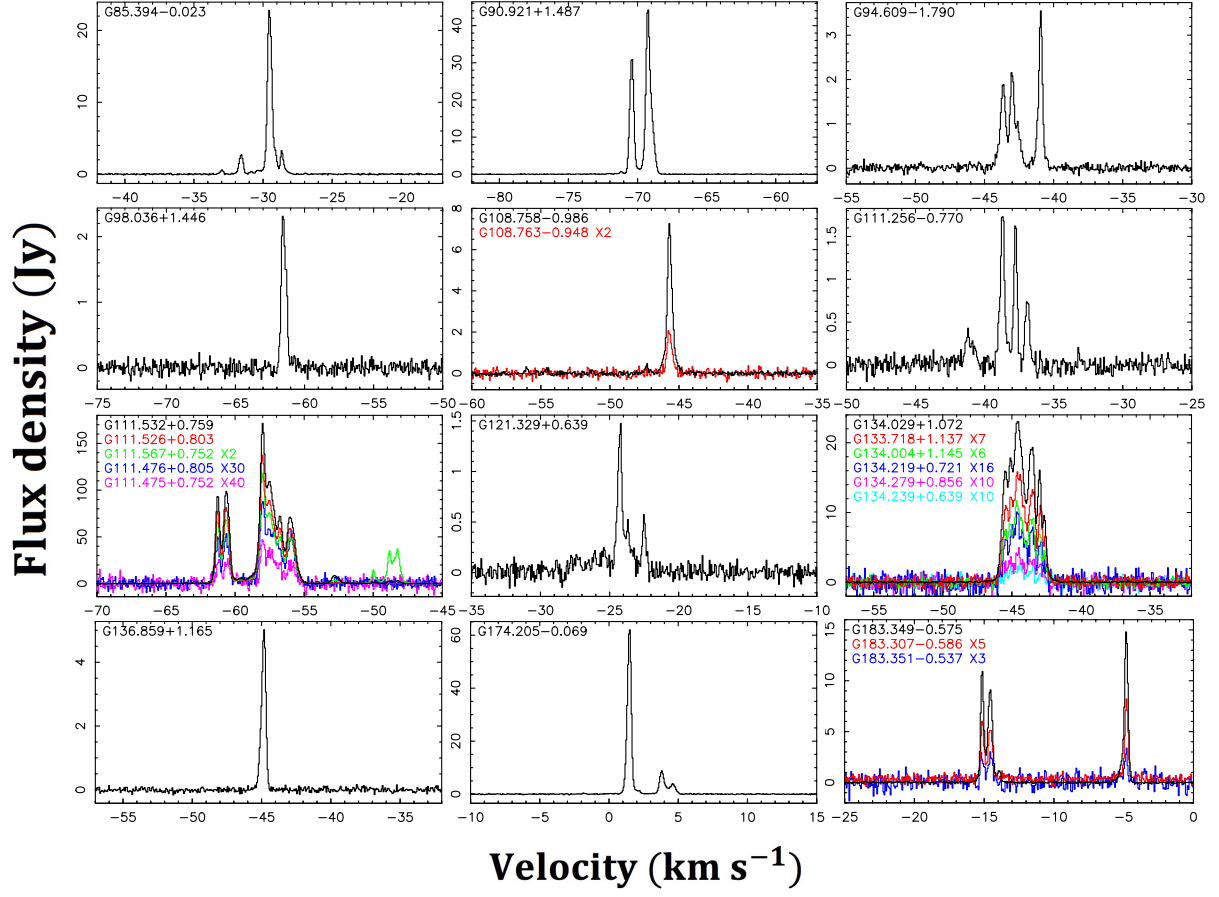


Fig. 2.— Continued

Fig. Set 3. Velocity-integrated intensity maps obtained with TRMR OTF observations and the spectra of the 6.7 GHz CH₃OH methanol masers

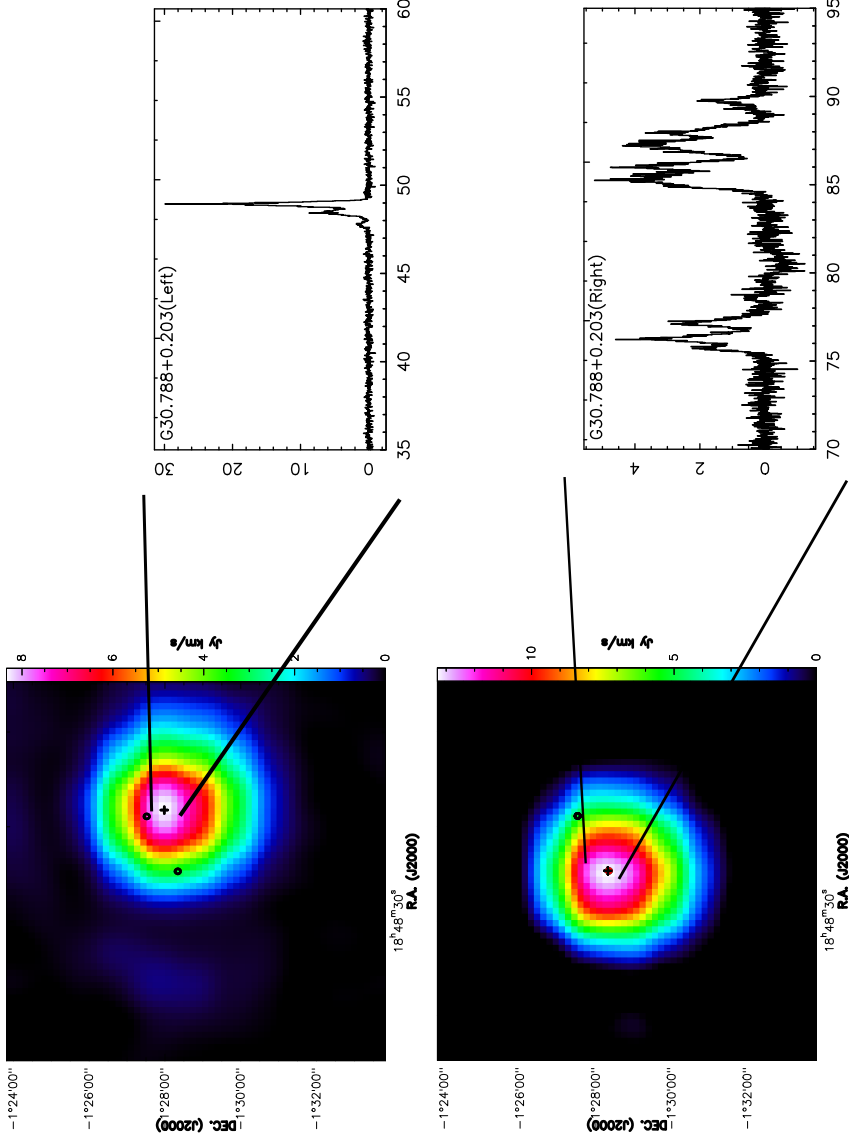


Fig. 3.— Velocity-integrated intensity maps obtained with TRMR OTF observations and the spectra of the 6.7 GHz CH_3OH methanol masers from G30.788+0.203 (upper) and G30.788+0.203 (lower). The “o” represents the position of the *WISE* source in the single-point-survey, and the “+” represents the fitted peak position of the CH_3OH emission from the TMRT OTF observation. The complete figure of 5 images is available online.

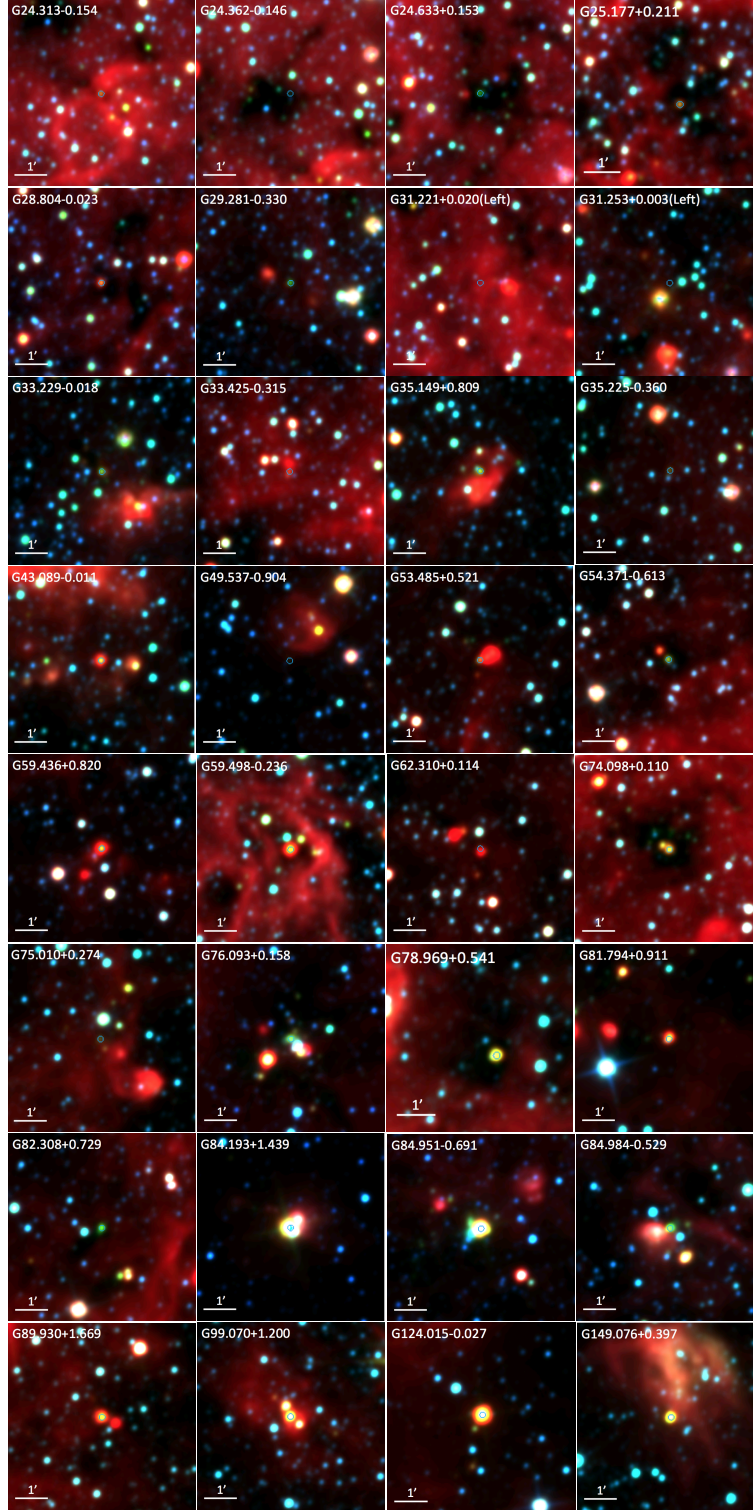


Fig. 4.— Infrared three-color images of the 32 newly detected methanol sources. The blue, green, and red colors represent 3.4, 4.6, and 12 μm bands in *WISE*. The blue “o” in the middle of each image represents the WISE source position used for the TMRT observations. The field of view of each region is a square with a side length of 6’.

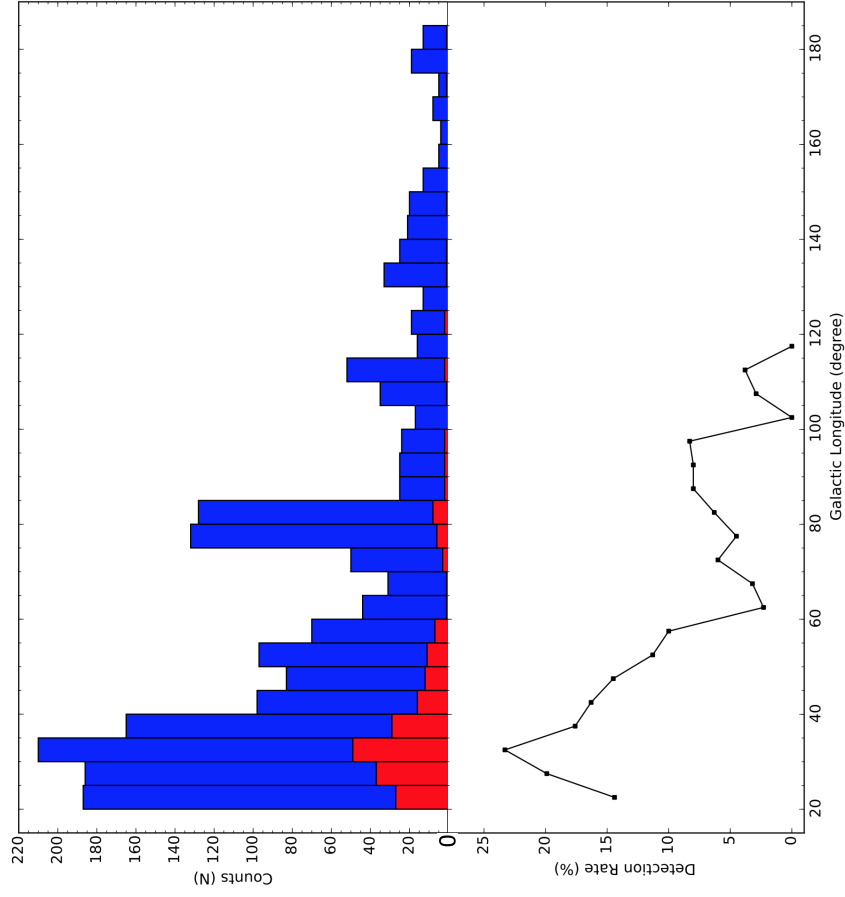


Fig. 5.— Upper panel: Histogram of the observing sample source number (blue) and the detected source number (red). Lower panel: detection rate (line chart) along every 5° Galactic longitude.

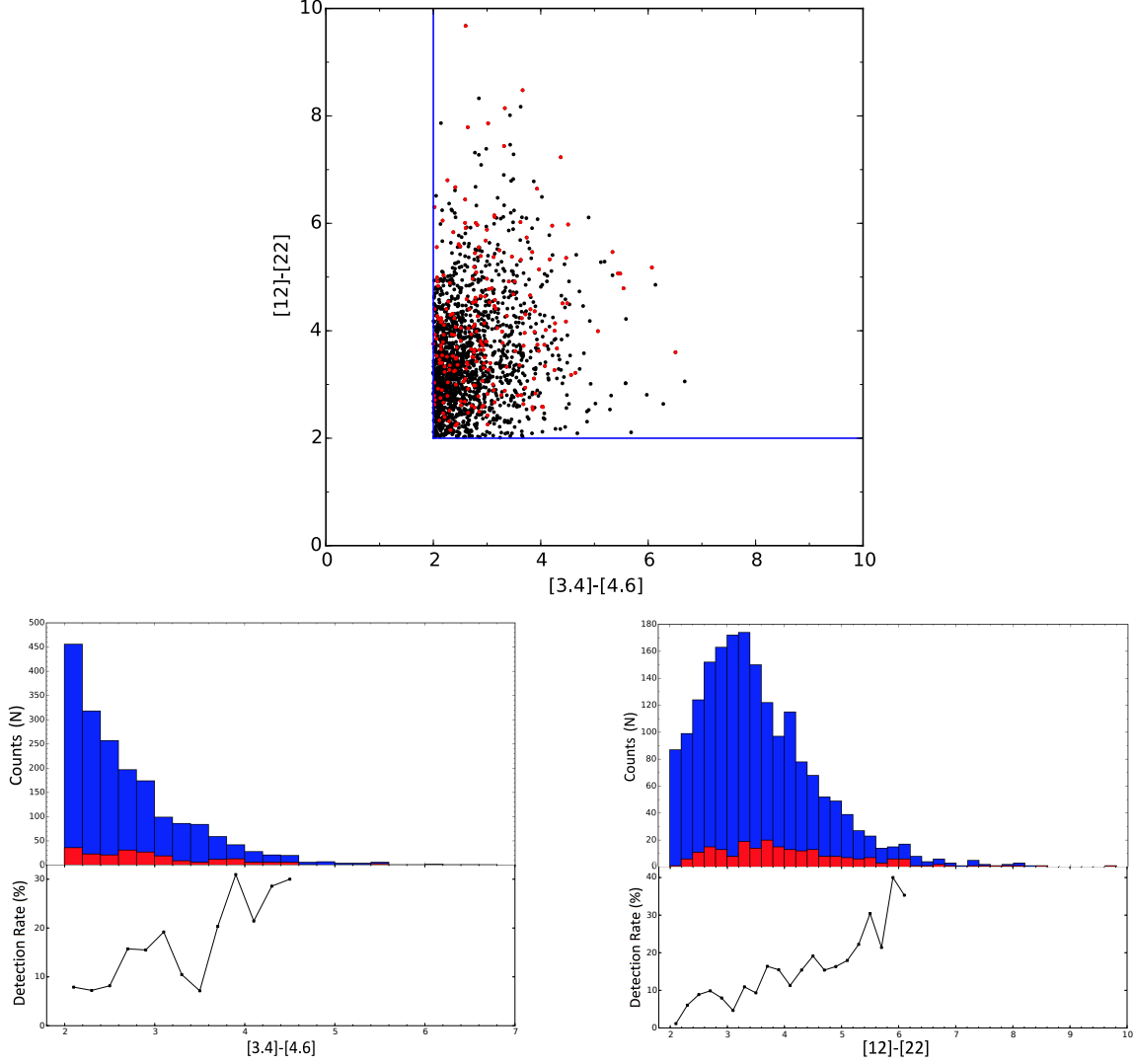


Fig. 6.— Upper panel: $[3.4]-[4.6]$ versus $[12]-[22]$ color of detected sources (red dots) and the 1875 observing sample sources (black dots) in our survey. Lower panels: the sample source numbers (histogram, blue), the detected source numbers (histogram, red) and detection rate (line chart) along every 0.2 color of $[3.4]-[4.6]$ (left) and $[12]-[22]$ (right).

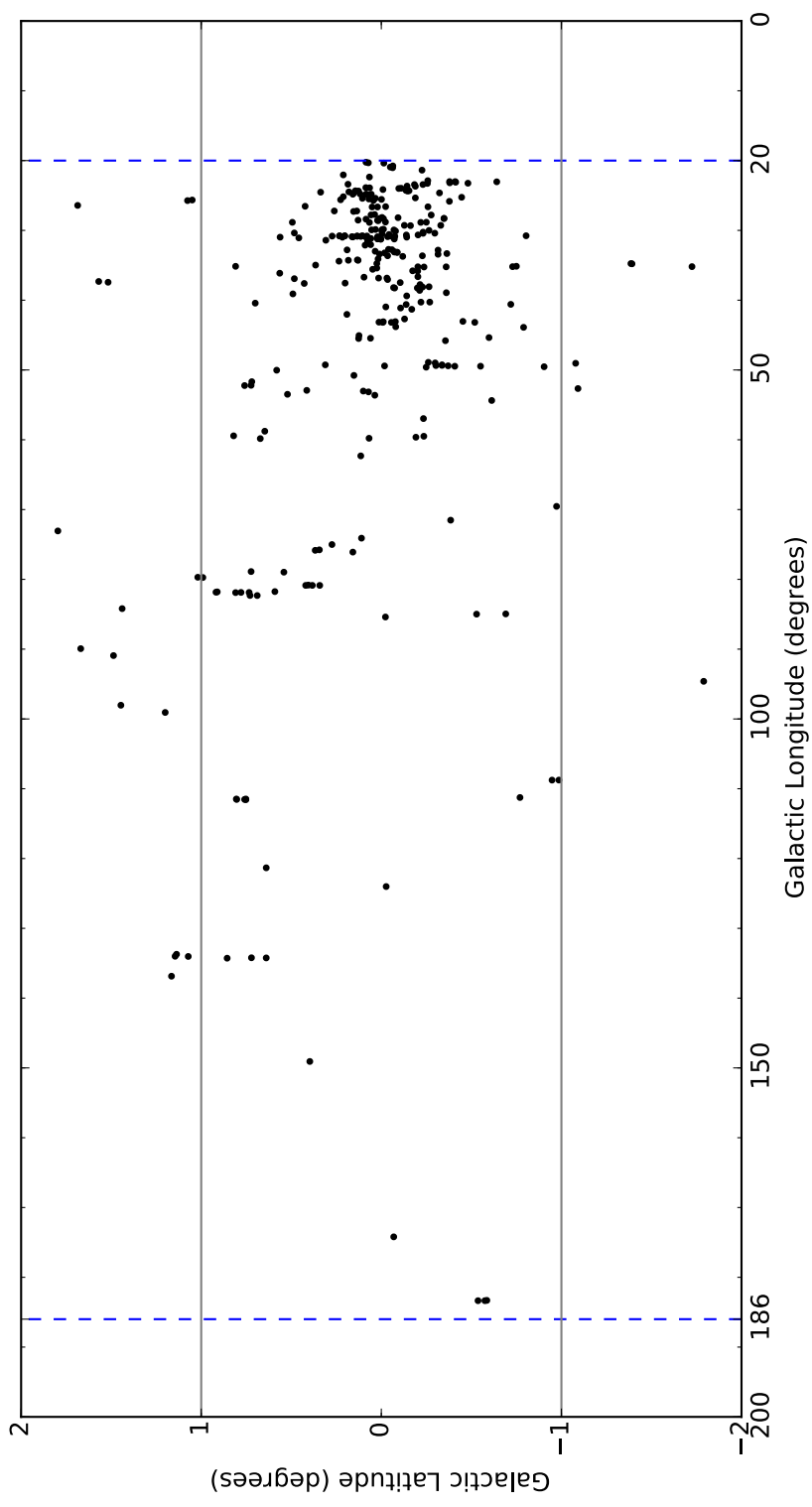


Fig. 7.— Galactic latitude distribution of the 224 6.7 GHz methanol maser sources detected by our TMRT survey at low latitude region, $20^\circ < |l| < 186^\circ$ and $|b| < 2^\circ$.

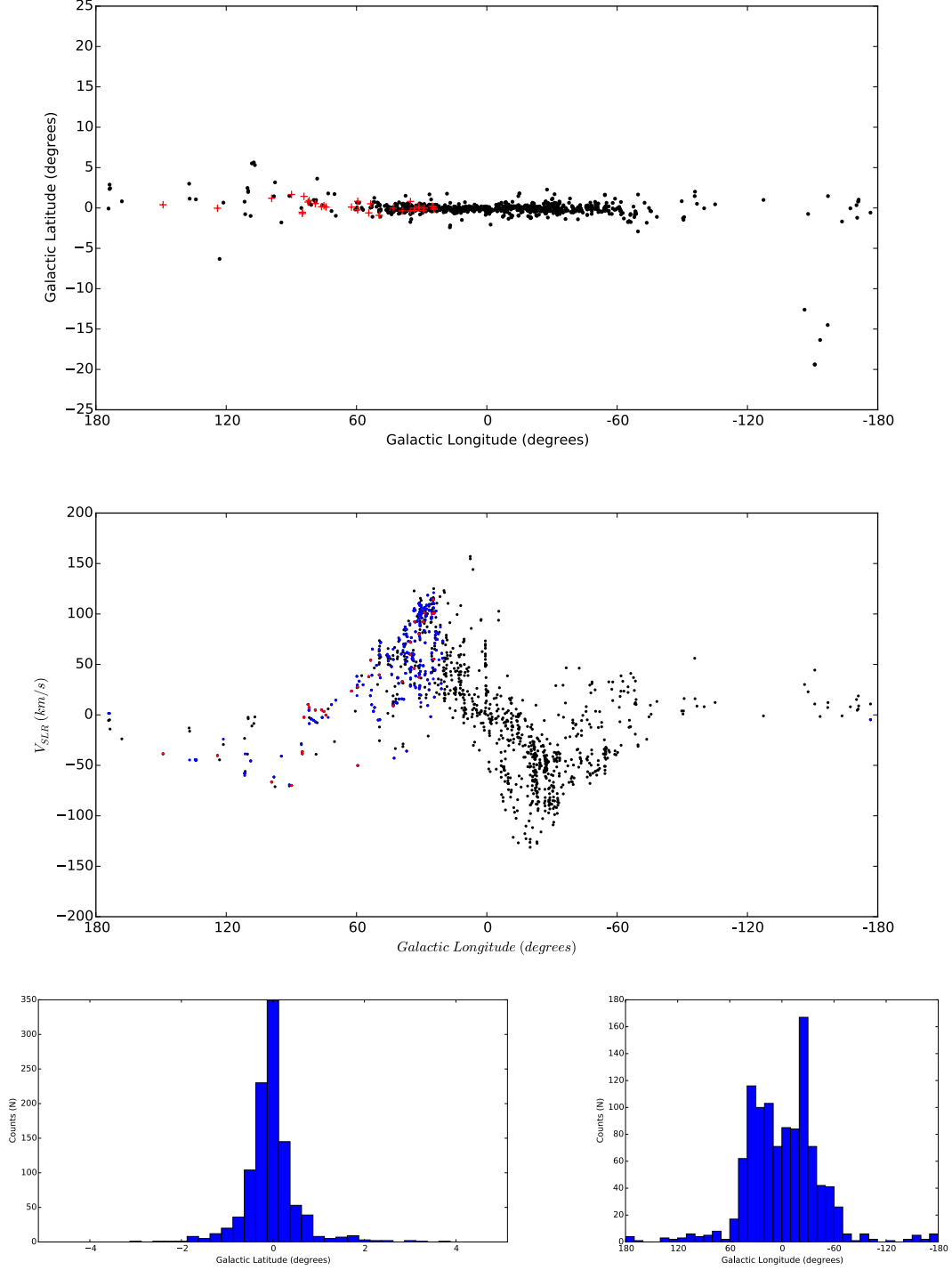


Fig. 8.— Top: Distribution of 1085 6.7 GHz methanol maser sources. The red “+” represents 32 newly detected sources in our survey. Middle: Distribution of the LSR velocities versus Galactic longitude. The blue dots represent the 224 detected sources in our survey and the red dots represent the 32 newly detected sources in our survey. Bottom: Source numbers versus galactic latitude, $|b| \leq 5^\circ$ (left panel), and galactic longitude (right panel).

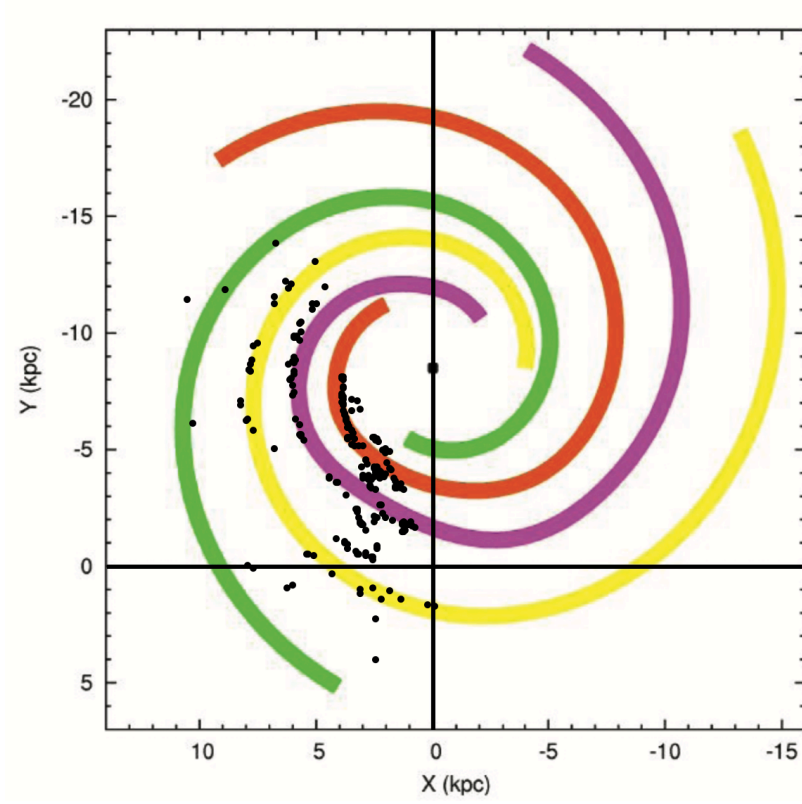


Fig. 9.— The black dots represent the positions of the detected sources in our survey. The Sun locates at the origin point $(0, 0)$. The spiral arms (yellow – Perseus; purple – Carina-Sagittarius; orange – Crux-Scutum; green – Norma) are illustrated same as Green et al. (2010).